



Modelling the dynamics of an oil drop driven by a surface acoustic wave in the underlying substrate

Mark Fasano^{1,†}, Yifan Li^{2,†}, Javier Alberto Diez³, Joseph D'Addesa, Ofer Manor², Linda Cummings and Lou Kondic b

Corresponding author: Lou Kondic, kondic@njit.edu

(Received 23 May 2025; revised 18 September 2025; accepted 3 October 2025)

We present a theoretical study, supported by simulations and experiments, on the spreading of a silicone oil drop under MHz-frequency surface acoustic wave (SAW) excitation in the underlying solid substrate. Our time-dependent theoretical model uses the long-wave approach and considers interactions between fluid dynamics and acoustic driving. While similar methods have analysed the micron-scale oil and water film dynamics under SAW excitation, acoustic forcing was linked to boundary layer flow, specifically Schlichting and Rayleigh streaming, and acoustic radiation pressure. For the macroscopic drops in this study, acoustic forcing arises from Reynolds stress variations in the liquid due to changes in the intensity of the acoustic field leaking from the SAW beneath the drop and the viscous dissipation of the leaked wave. Contributions from Schlichting and Rayleigh streaming are negligible in this case. Both experiments and simulations show that, after an initial phase where the oil drop deforms to accommodate acoustic stress, it accelerates, achieving nearly constant speed over time, leaving a thin wetting layer. Our model indicates that the steady speed of the drop results from the quasi-steady shape of its body. The drop speed depends on drop size and SAW intensity. Its steady shape and speed are further clarified by a simplified travelling-wave-type model that highlights various physical effects. Although the agreement between experiment and theory on drop speed is qualitative, the results' trend regarding SAW amplitude variations suggests that the model realistically incorporates the primary physical effects driving drop dynamics.

¹Department of Mathematical Sciences and Center for Applied Mathematics and Statistics, New Jersey Institute of Technology, Newark, NJ 07102, USA

²Department of Chemical Engineering, Technion – Israel Institute of Technology, Haifa 32000, Israel

³Instituto de Física Arroyo Seco, Universidad Nacional del Centro de la Provincia de Buenos Aires and CIFICEN-CONICET-CICPBA, Tandil 7000, Argentina

^T M. Fasano and Y. Li did a comparable amount of work, with Fasano focusing on modelling and simulations, and Li on experiments.

[©] The Author(s), 2025. Published by Cambridge University Press. This is an Open Access article, distributed under the terms of the Creative Commons Attribution licence (https://creativecommons.org/licenses/by/4.0/), which permits unrestricted re-use, distribution and reproduction, provided the original article is properly cited.

Key words: thin films, lubrication theory, acoustics

1. Introduction

Dynamic wetting of a solid substrate by a liquid film is a common occurrence. In natural systems, it appears in surfactant films that wet the lungs to promote breathing and the eyes to keep them moist (Holly & Lemp 1971; Veldhuizen & Haagsman 2000), or in the spreading of water drops on solid surfaces, such as raindrops on windows (Dussan V. & Davis 1974; Dussan V. & Chow 1983). In technological systems it is harnessed for actuating microfluidic platforms (Stone, Stroock & Ajdari 2004; Atencia & Beebe 2005; Whitesides 2006), for cooling electronic circuits (Amon et al. 2001; Bar-Cohen, Arik & Ohadi 2006), for desalination (Fletcher, Sernas & Galowin 1974) and for a variety of manufacturing applications (Fendler 1996; Nagayama 1996; Wang et al. 2004). Many different mechanisms govern dynamic wetting, where capillary forces at the free surface of a liquid film, or at a meniscus, contribute appreciably to the dynamics of the film. In addition to capillary forces, dynamic wetting may be powered by gravity, thermal or solutal Marangoni effects or electrokinetics, among other driving mechanisms; see Oron, Davis & Bankoff (1997) or Craster & Matar (2009) for comprehensive reviews. In the present work, we focus on the contributions of mechanical vibrations in the solid substrate, particularly MHz-frequency Rayleigh surface acoustic waves (SAWs), to dynamic wetting (Morozov & Manor 2018). We study particularly the effects of bulk acoustic streaming – mass transport in the bulk fluid that results from variations in acoustic intensity therein. While extensively observed and described in the scientific literature (Brunet et al. 2007, 2009; Yeo & Friend 2014), we are not aware of a model describing the dynamics of such a system that further accounts for the capillary and gravitational stresses that shape the liquid/air interface for the case when drops are sufficiently thick (millimetre scale, therefore much thicker than the SAW wavelength). Here, we use thin film (long wave) theory alongside physical experiments to develop a better understanding of the dynamics of this problem.

There are several different mechanisms by which acoustic waves or other mechanical waves, at a solid boundary or at the free surface of a liquid, generate streaming – steady flow along the wave's path. A mechanical wave at a boundary invokes periodic viscous flow within the viscous penetration length $\delta \equiv \sqrt{2\mu/(\rho\omega)}$ away from the interface, where μ , ρ and ω are the viscosity and density of the liquid, and the wave angular frequency, respectively. Examples in which this problem was considered include the work by Rayleigh on a standing acoustic wave grazing a solid bed (Rayleigh 1884); by Schlichting (1932) on standing vibration of waves of infinite and finite (respectively) wavelength in a solid along its surface; by Longuet-Higgins (1953) on shallow ocean waves; and by Manor, Yeo & Friend (2012) on propagating Rayleigh (surface acoustic) waves in a solid substrate. Convective contributions due to surface waves invoke a drift of liquid mass, which does not attenuate away from the solid surface. This is known as Schlichting streaming (Yeo & Friend 2014), and its component far from the boundary was further coined the 'Rayleigh law of streaming' by Lighthill (1978) in recognition of Rayleigh's work on the drift resulting from the presence of standing acoustic waves in fluid near a solid boundary.

A separate mechanism, the Eckart streaming, appears regardless of the presence of a boundary. This is an acoustic streaming that occurs in the bulk fluid, and results from variations in the intensity of sound or ultrasound waves in the fluid. In the classic work by Eckart and in many subsequent studies, acoustic streaming is ascribed to the viscous attenuation of travelling waves in the fluid (Eckart 1948; Nyborg 1952; Lighthill 1978). This attenuation results in spatial variations of the wave intensity in the fluid,

and in corresponding spatial variations in convective Reynolds stresses. The consequence is a secondary flow, whose steady component at long times is the acoustic streaming, characterised by an intense vortical flow field that appears in the bulk fluid. This is the main acoustic mechanism for the actuation of fluid in micro-channels (Wixforth 2003; Wixforth et al. 2004; Yeo & Friend 2014; Fasano et al. 2025) and in drop microfluidics (Guttenberg et al. 2004; Brunet et al. 2007, 2009, 2010). It usually dominates contributions to the flow in the bulk fluid arising from the boundary layer-type acoustic streaming mechanisms, such as Schlichting or Rayleigh streaming described above. An additional effect related to the interaction of acoustic waves with a surface, the acoustic radiation pressure (Hertz & Mende 1939; Hamilton & Blackstock 1998), may be also relevant in the presence of interfaces, such as the fluid-air surface. This effect has been discussed extensively in the literature (King 1934; Campbell 1970; Chu & Apfel 1982; Shiokawa, Matsui & Ueda 1989; Hasegawa et al. 2000; Borgnis 2010; Karlsen, Augustsson & Bruus 2016; Rajendran, Aravind & Subramani 2023), and shown capable of deforming and displacing soft interfaces and of governing the dynamics of films (Biwersi, Manceau & Bastien 2000; Alzuaga, Manceau & Bastien 2005; Issenmann et al. 2006; Rajendran et al. 2022; Marcos et al. 2025). Altshuler & Manor (2015) consider the problem of a partially wetting water drop atop a MHz frequency propagating vibration in the substrate, in a set-up similar to the one considered here, although the reduced viscosity and increased surface tension lead to reduced viscous dissipation of the leaky SAW in the fluid, and a necessity to include disjoining pressure to model liquid-solid interactions. Horesh et al. (2019) further consider a vertical set-up where gravity becomes important and show that acoustic radiation pressure is negligible for the partially wetting water due to the curvature of the meniscus, which does not support acoustical resonance.

While the literature discussing the interaction of acoustic waves with fluids is clearly extensive, in what follows, we discuss briefly just a few works that are particularly relevant in the present context, in which a SAW travelling in a solid substrate drives flow in a neighbouring fluid. In 1970, Campbell & Jones (1970) simulated a SAW in a piezoelectric solid in contact with an ideal (inviscid) fluid. Then, in the late 1980s, Shiokawa *et al.* (1989) used the ansatz of a harmonic acoustic waveform in the solid based on ideas developed by Nyborg (1952), converted the approach adopted by Campbell & Jones (1970) to analytic expressions and calculated the resulting acoustic forcing in the adjacent inviscid fluid due to attenuation of SAW in the solid. More recently, Vanneste & Bühler (2011) revisited the work of Campbell & Jones (1970) in the context of viscous fluids and calculated numerically the corresponding acoustic forcing in the fluid.

In the present paper, we focus on developing a model that can be used to formulate a long-wave theory applicable to the free surface evolution of thin viscous films and drops due to the presence of a SAW propagating in an underlying solid substrate. To facilitate such a development, we simplify the previously considered approaches in order to isolate the dominant physical effects governing the dynamics of the film. In particular, we simplify the approach used by Campbell & Jones (1970) by assuming damped harmonic waves in the solid. Furthermore, we compare the previous approaches by Vanneste & Bühler (2011) and Shiokawa *et al.* (1989) to quantify the importance of viscous effects, which were included by the former authors but ignored by the latter. We follow earlier attempts (Brunet *et al.* 2010) and focus on the contribution of acoustic streaming to the drop dynamics. In principle, one could also consider including the effects of the acoustic radiation pressure at the free surface, as was done in the recent work of Marcos *et al.* (2025), who used a Monte Carlo-type approach to study the dynamics of oil–water films under acoustic forcing. However, in the present case, the main contribution to drop displacement is the acoustic streaming, which efficiently transfers power from the SAW to the translational

motion of the drop; hence, we do not include acoustic radiation pressure here. This point will be discussed in further detail in § 3.

The rest of this paper is structured as follows. As a motivation, in § 2 we discuss simple physical experiments that demonstrate the well-known phenomenon of thick oil films and drops displacing under the action of MHz-frequency Rayleigh-type SAWs. These experiments illustrate the process of dynamic wetting and drop displacement powered by bulk acoustic streaming. We then derive the theoretical model that can explain such observations in § 3. Our theoretical results are presented in § 4: we discuss computational results in § 4.1, before analysing a simplified travelling—wave-type model in § 4.2. Sections 3 and 4, together with the appendices, constitute the main novel contributions of our work. Section 5 is devoted to the summary and conclusions. The appendices include (Appendix A) details of the theoretical results, (Appendix B) various simplifications and approximations including the inviscid limit and (Appendix C) the outline of the numerical approach implemented. Supplementary movies are available at https://doi.org/10.1017/jfm.2025.10802 provide videos of selected experiments and animations of representative computational results.

2. Experiment

The experiments described here are illustrative and portray the well-known phenomenon in which MHz-frequency SAWs are used to displace drops and thick films of liquid along the path of the SAW. The purpose of these experiments is to demonstrate the system under investigation, highlight key features and trends and provide results that will be used to motivate the theory and simulations presented in the following sections.

Figure 1 shows the experimental set-up (A) and a typical experimental result (a-e). We generate a propagating 20 MHz frequency SAW by applying a same-frequency sinusoidal voltage signal to a piezoelectric actuator – a SAW device. The actuator comprises a 5 nm titanium/1 µm aluminium interdigitated transducer (IDT; from which the SAW emanates) fabricated atop lithium niobate (LiNbO₃, Roditi International, UK) by standard lift-off photolithography. The substrate used for the SAW device is 11 mm × 24 mm in size, 0.5 mm thick, 128° Y-cut, X-propagating, single-crystal piezoelectric lithium niobate, where X and Y are crystal axes (Campbell & Jones 1968). The actuator is integrated into the external electrical signal using pogo pins (BC201403AD, Interconnect Devices, Inc.) assembled in a 3D-printed elastomeric stage, which holds the actuator and is connected to a signal generator (R&S SMB100A microwave signal generator) and amplifier (model A10160, Tabor Electronics Ltd.). Prior to the experiment we clean the SAW device using four different solvents: acetone (AR-b, 99.8 %, 67-641, Bio-Lab Ltd.), 2-propanol (AR-b, 99.8 %, 67-63-0, Bio-Lab Ltd.), ethanol (CP-p, 96 %, 64-17-5, Bio-Lab Ltd.) and water (HPLC plus, 7732-18-5, Sigma-Aldrich), before drying the actuator using compressed air. We place a paper cylinder soaked with glycerol at the far end of the actuator from the IDT to absorb the SAW and prevent reflections.

In our experiments, we represent the SAW strength (intensity) by measuring the normal displacement amplitude, A_n , at the solid surface before any attenuation in the liquid, so that A_n is the amplitude of the transverse component of the SAW in the substrate. We measure A_n over a surface of 1×1 mm² approximately 2 mm away from the SAW actuator using a scanning laser Doppler vibrometer (MSA-500, Polytech). We control this amplitude by changing the applied voltage, V, of the signal generator at the surface of the actuator: consistent with the literature (Ballantine *et al.* 1996), there is a linear relationship between A_n and V; see Li *et al.* (2025) for more details.

We place an $8\,\mu l$ ($8\,mm^3$) drop of silicone oil ($50\,cSt$, $378\,356$, Sigma-Aldrich) atop the actuator using a pipette, approximately $3.5\,mm$ away from the IDT, and introduce electrical

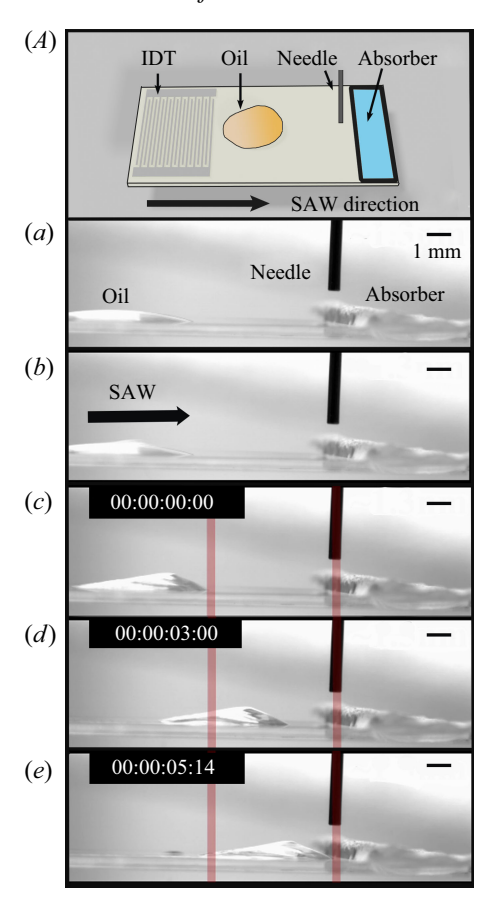


Figure 1. (A) Upper schematic view of the experimental set-up: SAW propagates from the IDT until it reaches the acoustic absorber (comprising glycerol-soaked paper placed on the actuator under and to the right of the needle). The needle is of known diameter $(510 \,\mu\text{m})$, placed for identifying spatial resolution in the images. (a–e) Successive snapshots are taken from an experiment monitoring the flow of a silicone oil film. During the experiment, a drop of silicone oil is placed on the horizontal surface (a), it deforms due to the application of SAW (b) and moves in the direction of SAW propagation (c–e); time is shown in seconds, and the vertical lines serve as a reference.

signal at different voltage levels to induce motion of the oil film, which dynamically wets the solid substrate along the path of the SAW. Figure 2(a-c) shows a time lapse (side view) of the typical silicone oil dynamics, captured using the framework and camera of a goniometer (Data Physics; OCA 15Pro). Figure 2(d) shows a top view obtained using a camera (EOS R5, Canon) with a macro lens (RF 100 mm F2.8L MACRO IS USM, Canon). To confirm that the observed dynamics is indeed induced by SAW, we also carried out control experiments, in which SAW is absent and all other parameters are kept the same. The oil drop in this experiment, which was repeated three times, slowly spreads concentrically, as expected in the absence of a directional forcing mechanism (figure not shown for brevity).

In the experiments with SAW actuation we employ the side-view video, recorded by a goniometer camera, to capture the position of the advancing three-phase contact line of the SAW-actuated oil film using the open-source software *Tracker* (Brown & Cox 2009) (see figure 3a for typical data). We also measure the maximum height of the moving oil film using *Tracker* (typical results in figure 3b). Figure 3(a) shows that, as expected, the larger

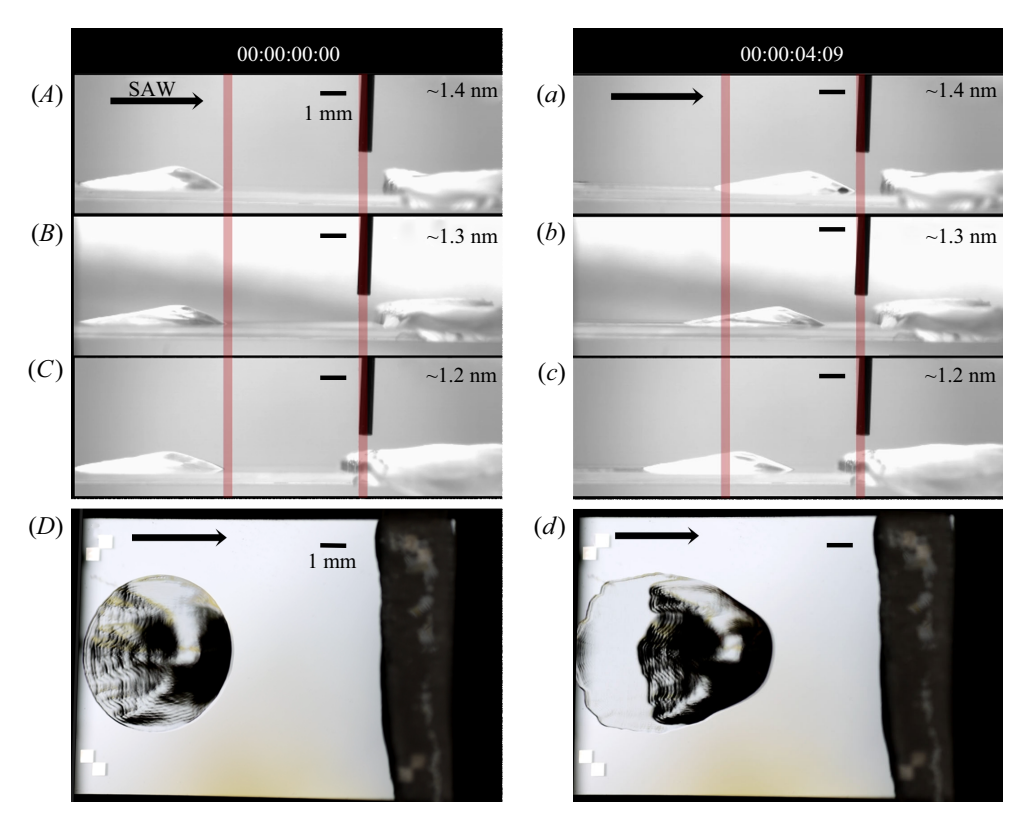


Figure 2. Two sets of images from experiments monitoring silicone oil drops powered by SAWs of three different measured amplitudes A_n (1.2–1.4 nm), where (A–C) silicone oil starts from the same location, moves in the direction of the SAW and reaches different distances (a–c) after 4.09 s. The corresponding side-view videos at different acoustic power levels are used to analyse the speed and profile of silicone oil during the movement. (D, d) Show top-view snapshots (corresponding to (C, c)) of the oil. A thin film of oil, hardly visible in the side view, can be seen more clearly behind the main body of silicone oil in the top views.

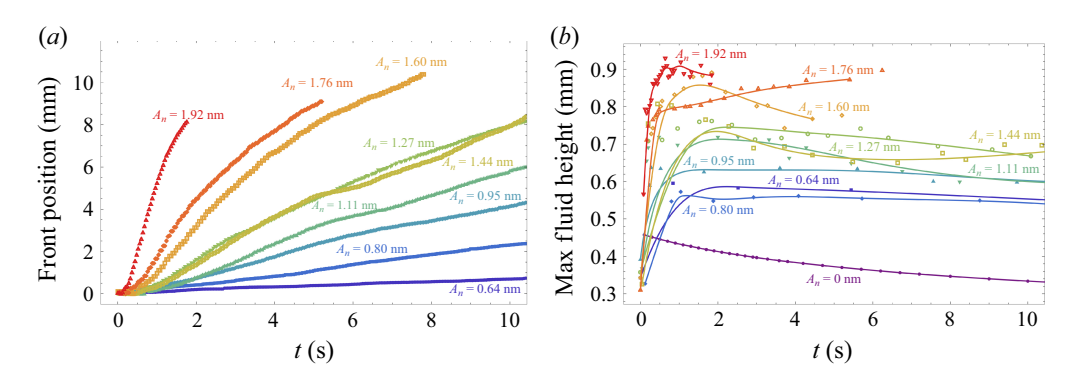


Figure 3. Time evolution of (a) the front position and (b) the maximum drop height for several values of A_n , for silicone oil drops of volume $\mathcal{V}_d = 8\,\mu\mathrm{l}$ and kinematic viscosity $\nu = 50\,\mathrm{cSt}$. The symbols correspond to the measurements, and the lines are simple fits to guide the eye. We expect errors of $\pm 50\,\mu\mathrm{m}$ in the values of the film height due to the limited resolution of the side-view image and tracker software. Note that t=0 corresponds to the time instant at which SAW is applied, which is 2 s after deposition of the oil. A video showing the evolution at various SAW amplitudes is available as a supplementary material (movie 1).

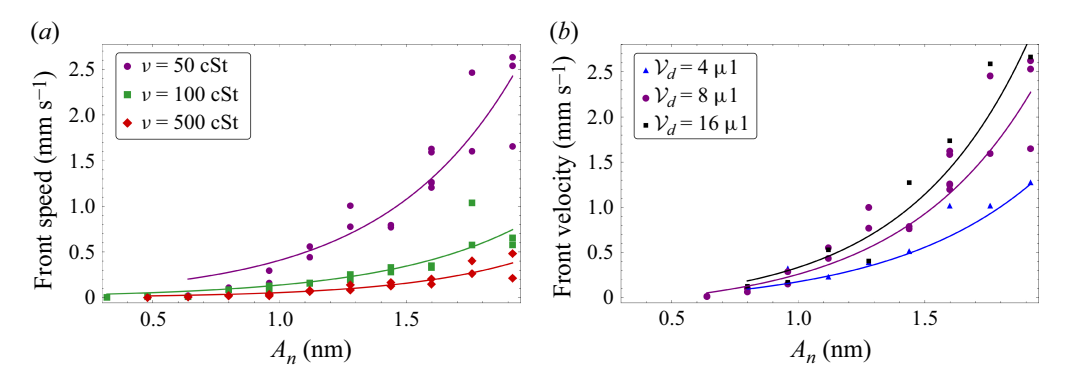


Figure 4. Asymptotic front speed of drop profiles for several values of the SAW amplitude A_n obtained using (a) silicone oil drops of volume $\mathcal{V}_d = 8 \,\mu l$ and different kinematic viscosities ν ; and (b) different volumes \mathcal{V}_d of silicone oil of the same viscosity $\nu = 50 \,\text{cSt}$. We present two example movies comparing typical evolution at various kinematic viscosities and volumes in the supplementary material (movie 2, movie 3).

the SAW amplitude A_n , the faster the oil film moves due to the stronger induced leakage wave (Shiokawa *et al.* 1989). Another notable aspect of SAW-induced dynamics is the contact line speed for early times (<1 s): initially, it is rather small, but later increases and then remains constant. This change of contact line speed appears to be a consequence of the initial change of shape of the drop (see also figure 1); while this is taking place, contact line speed is small. After the initial deformation, the drop shape remains unchanged, translating approximately uniformly. Figure 3(b) shows consistent results for the maximum drop height, with an increase in height for early times, and constant values for longer times. Note that this uniform translation and constant film height differ significantly from the observed behaviour for spreading under a body force such as gravity. These experimental observations will be explained and discussed within the framework of our theoretical model, which is described in the next section. We note that in our experiments, we do not observe drop oscillations as in the experiments using water drops (Brunet *et al.* 2010), possibly due to the much higher viscosity of the silicone oil.

In the experiments measuring the asymptotic front speed, we place a drop of silicone oil of various volumes (4/8/16 µl) and viscosities (50 cSt, 378 356, Sigma-Aldrich; 100 cSt, 378 364, Sigma-Aldrich; 500 cSt, 378 380, Sigma-Aldrich) on the SAW actuator in a similar manner. We then apply different levels of SAW to induce the movement of the oil film. The initial frames of recorded side-view videos are processed by public domain image processing software ImageJ to mark a known distance of 5 mm (see the red lines in figure 2(A-C) and movie 1, movie 2, movie 3 in the supplementary materials). The times at which the drop fronts pass these 5 mm markers are recorded. Since the marked area is positioned rather far from the IDT, we assume the drops have by this time settled to uniform translation, and we use these markers to calculate the average speed of the drops (of various volumes/viscosities); see figure 4(a-b). Figure 4(a) shows that front speed decreases as viscosity increases, assuming a fixed amplitude of the SAW. Interestingly, this decrease in front speed does not scale linearly with viscosity (as is the case for drops under the influence of only gravity and capillarity, i.e. drops sliding down a ramp or spreading on a flat substrate under capillary forces) due to the nonlinear dependence of the acoustic terms on the viscosity, which is discussed in the model formulation in § 3. Figure 4(b) shows that the front speed increases as drop volume increases, an effect that is magnified for larger SAW amplitudes.

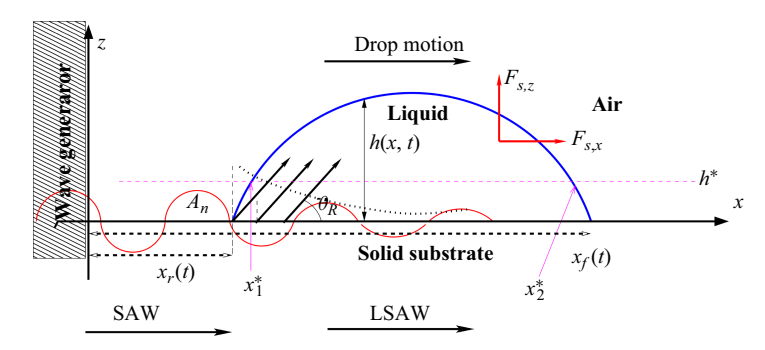


Figure 5. Schematic of a liquid drop (blue curve) driven by a leaky SAW (LSAW) of amplitude A_n . The SAW travels from left to right in the solid substrate. The drop extends from the rear to the front contact lines at $x_r(t)$ and $x_f(t)$, respectively. The thin red line represents the amplitude A_n of the SAW at the substrate and shows how it is attenuated due to the presence of the liquid (the black dotted line is the envelope of the decaying amplitude in the liquid). The Rayleigh angle is denoted by θ_R . The thickness h^* and the positions $x_{1,2}^*$ are defined later in the text, see (4.3).

3. Model

In our model development, we follow the approach of Vanneste & Bühler (2011) and Campbell & Jones (1970), implementing simplifications appropriate to our experiments. One important point is that, for the considered parameters, the dominant contributions to the Reynolds stress (responsible for the force driving the flow) arise from both the SAW attenuation in the solid, and from viscous damping of the leaked wave. The latter effects were not included by Shiokawa *et al.* (1989); we will comment in particular in Appendix B on the consequences of this difference.

We consider a two-dimensional Newtonian fluid layer occupying a domain in the (x, z)-plane, traversed by a sound wave generated by a Rayleigh-type SAW travelling in a neighbouring solid; see figure 5 for a sketch. We assume that the associated acoustic field Mach number, $M_a \equiv \omega A_n/c$ (where ω , A_n and c are the SAW angular frequency, characteristic normal displacement amplitude at the solid surface and the phase velocity of the acoustic field in the fluid, respectively) is small ($M_a \ll 1$), and that the velocity (v), pressure (p), and density (ρ) fields in the fluid can be written as

$$\mathbf{v} = \mathbf{v}_0 + \mathbf{v}_1 + \mathbf{v}_2 + \dots = \mathbf{v}_0 + M_a \, \bar{\mathbf{v}}_1 + M_a^2 \, \bar{\mathbf{v}}_2 + \dots ,$$

$$p = p_0 + p_1 + p_2 + \dots = p_0 + M_a \, \bar{p}_1 + M_a^2 \, \bar{p}_2 + \dots ,$$

$$\rho = \rho_0 + \rho_1 + \rho_2 + \dots = \rho_0 + M_a \, \bar{\rho}_1 + M_a^2 \, \bar{\rho}_2 + \dots ,$$
(3.1)

where the leading-order components of these fields are associated with quiescent liquid ($v_0 = 0$, p_0 constant) of constant ambient density ρ_0 ; the first-order corrections (v_1 , p_1 , ρ_1), represent an oscillatory flow associated with the acoustic field generated by the SAW that average to zero over the period of the acoustic forcing; and the second-order corrections (v_2 , v_2 , v_2) represent the induced steady streaming flow. The assumption implicit in the above expansions in the Mach number is that the barred quantities are comparable in size to the corresponding leading-order contributions. The problem is governed by the Navier–Stokes and continuity equations,

$$\frac{\partial(\rho \mathbf{v})/\partial t + \rho (\mathbf{v} \cdot \nabla) \mathbf{v} + \mathbf{v} \nabla \cdot (\rho \mathbf{v})}{= -\nabla p + \mu \nabla^2 \mathbf{v} + (\mu_b + \mu/3) \nabla (\nabla \cdot \mathbf{v}) + \rho \mathbf{g},}$$
(3.2)

$$\partial \rho / \partial t + \nabla \cdot (\rho \mathbf{v}) = 0,$$
 (3.3)

where t is time; μ , μ_b are the shear and dilatational coefficients of the bulk viscosity, respectively; and $\mathbf{g} = -g\mathbf{e}_z$ is the gravitational acceleration. In terms of the above expansions, we will assume that the gravitational term does not appear until second order in M_a , which amounts to an assumption that $\mu v_1/\ell^2 \gg \rho g$ (where v_1 is a representative value of $|\mathbf{v}_1|$ and ℓ is a representative droplet size), ensuring that gravity is negligible in both leading-order and first-order problems. This condition was checked *a posteriori* and found to hold. With these assumptions, we substitute the expansions from (3.1) into (3.2) and collect terms of like orders in M_a ; §§ 3.1 and 3.2 discuss the first- and second-order terms, respectively.

3.1. First-order solution

The first order is associated with the propagation of acoustic waves in the fluid and hence we use the Helmholtz decomposition to separate the flow field into irrotational and divergence-free flow, i.e. $v_1 = \nabla \phi + \nabla \times \Psi$, where ϕ is the velocity potential of the irrotational flow component, and Ψ represents the divergence-free flow component, so that the flow vorticity is equal to $-\nabla^2\Psi$. We ignore contributions from Ψ , assuming $v_1 \approx \nabla \phi$. (The vorticity is known to be concentrated mainly in a boundary layer flow near the solid surface of thickness $\sqrt{\mu/(\rho_0\omega)}$, which amounts to just a few hundred nanometres and introduces only small contributions to the bulk flow far from the solid compared with the acoustic wave described by the potential ϕ ; see Vanneste & Bühler (2011) for a general approach that further accounts for the boundary layer flow.) Here and in the following, it is understood that the real part of complex equations is taken when presenting results for real quantities such as ϕ , v_1 or v_2 .

For simplicity of notation we then set $v_1 = \nabla \phi$ in (3.1), leading (at order M_a on substitution in (3.2) and (3.3)) to the damped wave equation (Vanneste & Bühler 2011)

$$\phi_{tt} = c^2 \nabla^2 \phi + (\nu + \nu') \nabla^2 \phi_t, \tag{3.4}$$

where $c^2 = \mathrm{d}p/\mathrm{d}\rho|_0$, $v' = v_b + v/3$, with $v \equiv \mu/\rho_0$ and $v_b \equiv \mu_b/\rho_0$. Assuming that the potential function, ϕ , is harmonic in time with angular frequency ω , and hence given by $\phi = \hat{\phi}(x) \exp(i\omega t)$, (3.4) may be reduced to

$$\nabla^2 \hat{\phi} = -\frac{\omega^2}{c^2 + i(\nu + \nu')\omega} \hat{\phi} = -\kappa^2 \hat{\phi}, \tag{3.5}$$

where

$$\kappa = \frac{k}{\sqrt{1 + i(\nu + \nu')k/c}},$$
(3.6)

and $k = \omega/c = 2\pi/\lambda$ is the wavenumber of the sound wave in the liquid, with wavelength λ . The real and imaginary parts of κ are given by

$$\kappa = k_r - i \ k_i = k \sqrt{\cos \beta} \ e^{-i\beta/2}, \tag{3.7}$$

assuming $\beta \in (0, (\pi/2))$ where

$$\tan \beta = (\nu + \nu') \frac{k}{c}.\tag{3.8}$$

The solution of (3.5) requires a boundary condition that captures the corresponding leading-order behaviour for the normal component of a Rayleigh-type SAW at the solid surface. This condition can be derived from the solution given by Royer & Dieulesaint

Physical parameters	Wave parameters	Lengths in substrate	Lengths in oil
$ \rho_0 = 0.96 \mathrm{g cm^{-3}} $ $ \nu = \nu' = 50 \mathrm{cSt} $ $ \gamma = 20.8 \mathrm{dyn cm^{-1}} $ $ c = 1350 \mathrm{m s^{-1}} $ $ \rho_s = 4.65 \mathrm{g cm^{-3}} $ $ c_s = 3880 \mathrm{m s^{-1}} $ $ \ell = 1 \mathrm{mm} $	f = 20 MHz $\omega = 125.7 \text{ MHz}$ A = 1.04 - 10 nm $A_n = 0 - 1.69 \text{ nm}$	$k_{s,r}^{-1} = 0.03 \text{ mm}$ $k_{s,i}^{-1} = 2.70 \text{ mm}$ $\lambda_s = 194 \mu\text{m}$ $\delta = 0.91 \mu\text{m}$	$k_r^{-1} = 0.01 \text{ mm}$ $k_i^{-1} = 2.56 \text{ mm}$ $\lambda = 67.5 \mu \text{m}$

Table 1. Values of the physical parameters related to the experiments and the derived lengths for both the solid substrate and the liquid (PDMS).

(1996) for the Rayleigh wave in an isotropic solid as

$$\left. \frac{\partial \phi}{\partial z} \right|_{z=0} = A\omega \exp(i\omega t) \exp(-i\kappa_s x),$$
 (3.9)

where subscript s stands for solid, and A is the displacement amplitude in the liquid. Unlike the solution in Royer & Dieulesaint (1996), the wavenumber κ_s has an imaginary part, i.e.

$$\kappa_s = k_{s,r} - ik_{s,i},\tag{3.10}$$

due to the presence of the liquid on top of the solid that converts the simple SAW into a LSAW. The consequent attenuation of the LSAW is accounted for by the imaginary part of κ_s , which is given by (Arzt, Salzmann & Dransfeld 1967)

$$k_{s,i} = \frac{\rho_0}{\rho_s} \frac{c}{c_s^2} f,$$
 (3.11)

where ρ_s is the solid density, $f = \omega/2\pi$ is the SAW frequency and c_s (= $\omega/k_{s,r}$) is the SAW phase velocity in the substrate. Note that the boundary condition, (3.9), is derived using the expansion of the nonlinear Rayleigh wave for small strains in the solid, so that the actual deformations at the solid surface as well as the inherently nonlinear relation between strain and stress in the solid, contribute at higher orders of M_a , not considered here.

We comment here also on the relation between the experimentally measured amplitude, A_n , and the theoretical one, A, used in (3.9). Although we expect $A \propto A_n$, it is not clear that these amplitudes are identical, as discussed in some detail by Royer & Dieulesaint (1996). A detailed analysis to determine the exact relation between A and A_n is beyond the scope of the present work, so we assume that $A = A_n$, a point to which we return later when discussing the comparison between experimental and theoretical results.

The experimental parameter values relevant to the silicone oil–lithium niobate system that we consider here are summarised in table 1. Note that, for the considered experimental parameters, we have $\tan \beta \approx \beta \ll 1$ or $\nu + \nu' \ll c/k$, so that to leading order in β (see (3.7), (3.8))

$$k_r \approx k, \quad k_i \approx k \frac{\beta}{2} \approx \frac{k^2 \left(\nu + \nu'\right)}{2c}.$$
 (3.12)

This approximate value of k_i is in agreement with that defined in (5) of Brunet *et al.* (2010). Note that $\beta \ll 1$ for a range of fluids; e.g. for water ($\nu = 1$ cSt) and oil ($\nu = 50$ cSt) we obtain $\beta = 1.67 \times 10^{-4}$ and $\beta = 8.38 \times 10^{-3}$, respectively, assuming $\nu_b = \nu$ in

both cases. Therefore, we can consider the ratio k_i/k_r as a small parameter, as discussed further in Appendix B.

The problem prescribed by (3.5) and (3.9), alongside a requirement that the acoustic field velocity decays far from the solid surface as $z \to \infty$, is satisfied by the potential function

$$\phi = \frac{-A\omega}{\sqrt{\kappa_s^2 - \kappa^2}} \exp(i\omega t) \exp(-i\kappa_s x) \exp\left(-z\sqrt{\kappa_s^2 - \kappa^2}\right), \tag{3.13}$$

yielding the velocity components

$$v_{1,x} = \frac{\partial \phi}{\partial x} = \frac{i\kappa_s}{\sqrt{\kappa_s^2 - \kappa^2}} A\omega \exp(i\omega t) \exp(-i\kappa_s x) \exp\left(-z\sqrt{\kappa_s^2 - \kappa^2}\right),$$

$$v_{1,z} = \frac{\partial \phi}{\partial z} = A\omega \exp(i\omega t) \exp(-i\kappa_s x) \exp\left(-z\sqrt{\kappa_s^2 - \kappa^2}\right).$$
(3.14)

For reference, the (physically relevant) real parts of these velocity components are written out explicitly in Appendix A.

We note that the analysis presented so far follows parts of the work by Campbell & Jones (1970) and Vanneste & Bühler (2011), albeit instead of calculating the SAW in the solid from conservation equations, we take the simpler approach of representing the component of the LSAW at the solid surface as a harmonic function that decays exponentially along its path (Arzt *et al.* 1967) and hence are able to obtain the analytical representation of the acoustic contribution to the velocity field in the fluid. The formulation that ignores viscous dissipation is discussed in Appendix B.

3.2. Second-order solution

Having obtained v_1 , we next seek the quasi-steady flow field at times long compared with the acoustic period (Stokes 1847; Rayleigh 1884; Schlichting 1932). Since we excite the fluid using a single-frequency SAW, it is sufficient to time average the system of equations over the period of the SAW (Vanneste & Bühler 2011) using the operator $\langle \cdot \rangle \equiv \omega/(2\pi) \int_{t=0}^{2\pi/\omega} \cdot dt$. The leading-order velocity contribution that supports a steady flow component (and hence does not vanish) is $\langle v_2 \rangle$, appearing at order M_a^2 in the expansions specified by (3.1). The corresponding conservation of momentum and mass equations are then given by

$$-\nabla \langle p_2 \rangle + \mathbf{F}_s - \rho_0 g \mathbf{e}_z + \mu \nabla^2 \langle \mathbf{v}_2 \rangle + \left(\mu_b + \frac{\mu}{3}\right) \nabla \left(\nabla \cdot \langle \mathbf{v}_2 \rangle\right) = 0, \tag{3.15}$$

$$\rho_0 \nabla \cdot \langle \mathbf{v}_2 \rangle + \nabla \cdot \langle \rho_1 \mathbf{v}_1 \rangle = 0, \tag{3.16}$$

where

$$\mathbf{F}_{s} = -\langle \rho_{0} \left(\mathbf{v}_{1} \cdot \nabla \right) \mathbf{v}_{1} + \mathbf{v}_{1} \nabla \cdot (\rho_{0} \mathbf{v}_{1}) \rangle, \tag{3.17}$$

represents the acoustic force on the induced steady streaming flow. Moreover, considering the component of the continuity equation proportional to M_a , $\partial \rho_1/\partial t + \rho_0 \nabla \cdot v_1 = 0$ and the solution for v_1 specified by (3.14), we see that the product $\rho_1 v_1$ leads to an odd function over the SAW period, which results in $\langle \rho_1 v_1 \rangle = 0$. Hence, (3.15) and (3.16) may be simplified to

$$-\nabla \langle p_2 \rangle + \mathbf{F}_s - \rho_0 g \mathbf{e}_z + \mu \nabla^2 \langle \mathbf{v}_2 \rangle = 0, \tag{3.18}$$

$$\nabla \cdot \langle \mathbf{v}_2 \rangle = 0, \tag{3.19}$$

with F_s as specified in (3.17). In Appendix A we use the real part of the first-order velocity field, v_1 , to reveal the form of the SAW forcing as given in (3.17) above, and in Appendix B we discuss a simplified version as well as the inviscid limit. The main points we emphasise are that the acoustic streaming force, given by (3.17), is non-conservative in contrast to the result in Shiokawa *et al.* (1989), and that its prefactor is significantly dependent on the presence of viscous dissipation. The discussion is made explicit in Appendix A where the real component is shown along with the exact form of the coefficients therein.

3.3. Long-wave approximation

We carry out a standard long-wave expansion of (3.18) and (3.19), focusing on the simplified two-dimensional geometry that assumes translational invariance in the transverse y-direction ($\partial/\partial y = 0$). The discussion of three-dimensional effects will be presented elsewhere. Here, we obtain the pressure, $p \equiv \langle p_2 \rangle$, by substituting the z-component of F_s , given in (A7) and (A8), in the z-component of (3.18). We then integrate the resulting equation over the film thickness with respect to z, using the Laplace pressure boundary condition $p(x, h(x, t)) = -\gamma h''$ (simplifying the curvature of the free surface in the spirit of the long-wave approximation, and using to denote $\partial/\partial x$), to find

$$p(x,z) = -\gamma h'' + \rho_0 g(h-z) + \frac{C_z P_0}{2K_z} \left[\psi(x,h) - \psi(x,z) \right], \tag{3.20}$$

where parameters K_z , C_z are specified in (A6), (A10) respectively, and we defined the auxiliary function ψ and parameter P_0 as

$$\psi(x, z) = e^{-2(k_{s,i}x + K_z z)}, \qquad P_0 = \rho_0 A^2 \omega^2.$$
 (3.21)

The last term on the right-hand side of (3.20) is the contribution of the bulk acoustic forcing to the local pressure in the film. To obtain the velocity component in the *x*-direction at this order, $v_{2,x}$, we substitute both the *x*-derivative of the pressure in (3.20), and $F_{s,x}$ as given in (A7), into the *x*-component of (3.18). We then integrate twice with respect to *z*, applying a zero shear-stress boundary condition at the free surface $(\partial v_{2,x}/\partial z = 0)$ at z = h and a no-slip condition at the substrate $(v_{2,x} = 0)$ at z = 0, which yields

$$v_{2,x} = -\frac{1}{2\mu}z(z - 2h) \left[\gamma h''' - \rho_0 g h' + C_z P_0 \psi(x, h) \left(\frac{k_{s,i}}{K_z} + h' \right) \right] - C \frac{P_0}{4\mu K_z^3} e^{-2k_{s,i}x} \left(e^{-2K_z z} + 2K_z e^{-2K_z h} z - 1 \right),$$
(3.22)

where

$$C = K_z C_x - k_{s,i} C_z, \tag{3.23}$$

with parameter C_x defined in (A9). Note that the last term in (3.22) leads to a velocity profile $v_{2,x}$ that is modified from the usual parabolic shape in the neighbourhood of z = 0. Interestingly, there is a critical value of C, namely $C_{crit} < 0$, such that for $C < C_{crit}$, the velocity profile includes negative values of $v_{2,x}$ in the region near the substrate. We have not, however, observed such flow inversion with the present choice of parameters relevant to our experiments.

From the velocity profile above, (3.22), we obtain the film-averaged velocity and flux as

$$u = \frac{1}{h} \int_{0}^{h} v_{2,x} \, dz, \quad Q = uh.$$
 (3.24)

Conservation of mass for the fluid then requires that

$$\frac{\partial h}{\partial t} + \frac{\partial Q}{\partial x} = 0. {(3.25)}$$

Upon using the velocity profile as obtained in (3.22) above, we find

$$Q = -\frac{h^3}{3\mu} \frac{\partial \mathcal{P}}{\partial x} - \mathcal{C} \frac{P_0}{8\mu K_z^4} \psi(x, h) \left[2K_z^2 h^2 - 1 + e^{2K_z h} \left(1 - 2K_z h \right) \right], \tag{3.26}$$

where we have defined the effective pressure

$$\mathcal{P} = -\gamma h'' + \rho_0 g h + \frac{C_z P_0}{2K_z} \psi(x, h). \tag{3.27}$$

The first term on the right-hand side of \mathcal{P} is the capillary contribution to the quasi–steady pressure in the fluid film, wherein γ is the surface tension at the fluid–air interface, assumed constant; the second and third terms account for the gravitational body force; and the final term models the contribution from the acoustic force due to the SAW.

For our simulations, we non-dimensionalise the problem using an arbitrary length scale, ℓ , a time scale $t_c = 3\mu\ell/\gamma$ such that leading-order terms balance in (3.25), and a pressure scale $p_c = \gamma/\ell$ based on the capillary contribution in (3.27), so that we have

$$(x,h) = \ell(\tilde{x},\tilde{h}), \quad t = \frac{3\mu\ell}{\gamma}\tilde{t}, \quad \mathcal{P} = \frac{\gamma}{\ell}\tilde{\mathcal{P}},$$

$$(k_{s,i}, K_z, C_x, C_z) = \ell^{-1}(\tilde{k}_{s,i}, \tilde{K}_z, \tilde{C}_x, \tilde{C}_z), \mathcal{C} = \ell^{-2}\tilde{\mathcal{C}}.$$
(3.28)

Therefore, in dimensionless form, we have

$$\frac{\partial \tilde{h}}{\partial \tilde{t}} + \frac{\partial}{\partial \tilde{x}} \left[-\tilde{h}^3 \frac{\partial \tilde{\mathcal{P}}}{\partial \tilde{x}} - \tilde{\mathcal{C}} \frac{3S}{8\tilde{K}_z^4} \psi(\tilde{x}, \tilde{h}) \left(2\tilde{K}_z^2 \tilde{h}^2 - 1 + e^{2\tilde{K}_z \tilde{h}} \left(1 - 2\tilde{K}_z \tilde{h} \right) \right) \right] = 0, \quad (3.29)$$

where it is understood that in calculating $\psi(\tilde{x}, \tilde{h})$ we use (3.21) with $k_{s,i}$, K_z replaced by their tilded equivalents; the dimensionless effective pressure is

$$\tilde{\mathcal{P}} = -\tilde{h}'' + Bo\,\tilde{h} + \frac{\mathcal{S}\tilde{C}_z}{2\tilde{K}_z}\psi(\tilde{x},\,\tilde{h}),\tag{3.30}$$

and we have defined the non-dimensional parameters

$$Bo = \frac{\rho_0 g \ell^2}{\gamma} = \frac{\ell^2}{a^2}, \quad S = \frac{P_0 \ell}{\gamma} = \frac{\rho_0 \ell A^2 \omega^2}{\gamma},$$
 (3.31)

where $a = \sqrt{\gamma/(\rho_0 g)}$ is the capillary length. In our simulations, motivated by a typical drop size in the experiments, we set $\ell = 1$ mm. Table 2 provides a list of non-dimensional parameter values used in all simulations unless otherwise stated.

We pause here to provide a justification for neglecting the effects of acoustic radiation pressure in the present model. The experiments modelled here involve a SAW propagating in the solid with attenuation length of 1–2 mm, while the drops considered are 6–7 mm in lateral length. When comparing the relative strengths of acoustic streaming and acoustic radiation pressure, an important distinction is that streaming results from the SAW in the solid, while acoustic radiation pressure results from the LSAW in the liquid that reflects off the drop's free surface. The attenuation lengths of both effects are proportional to the relative phase velocities of the acoustic fields in the solid and fluid, respectively. Since the speed of sound in the liquid is 2–3 times smaller than the speed of sound in the solid,

Parameter	Definition	Numerical value	Physical meaning
${\mathcal S}$	$(\rho_0 \ell A^2 \omega^2)/\gamma$	0.788 - 72.88	Ratio of acoustic force and surface tension
Bo	$(\rho_0 g \ell^2)/\gamma$	0.452	Bond number
$ ilde{\mathcal{C}}$	$\tilde{K}_z \tilde{C}_x - \tilde{k}_{s,i} \tilde{C}_z$	-0.11	Effect of non-conservative SAW force
$rac{ ilde{K}_z}{ ilde{h}^*}$	See (3.28), (A6)	0.279	Attenuation coefficient of SAW in z
$ ilde{h}^*$	$(\lambda/4)/\ell$	0.017	Cutoff thickness at which attenuation begins
$ ilde{C}_z$	See (3.28), (A10)	0.415	Coefficient of z component of SAW force
$ ilde{ ilde{C}}_z \ ilde{ ilde{\mathcal{A}}}_d$	$(4/3)\tilde{h}_d\tilde{r}_d$	2.12	Area of drop
$ ilde{h}_d$	$(2\tilde{\mathcal{V}}_d)/(\pi \tilde{r}_d^2)$	0.497	Height of drop
\tilde{r}_d	a a a a a a a a a a a a a a a a a a a	3.2	Radius of drop
$ ilde{ ilde{h}}_p$		0.01	Precursor film thickness

Table 2. Dimensionless parameters used in the simulation of the experiment for a drop volume of $V_d = 8 \,\mu\text{I}$ driven by a SAW with A in the range from table 1, which determines the range of S.

the radiation pressure attenuates twice as fast as the SAW in the solid. Hence, the radiation pressure affects the drop rear only along a distance of approximately 0.5–1 mm. Because the present focus is on describing the front dynamics of driven drops, we neglect this contribution. However, we note that in cases where the attenuation length of the SAW is comparable to the lateral length of the drop, acoustic radiation pressure is expected to have an effect on the drop geometry and dynamics comparable to that of acoustic streaming, and hence should be included (see, e.g. Marcos *et al.* 2025). To quantify the regime in which radiation pressure becomes important, some insight can be reached by considering the non-dimensional ratio

$$R = \frac{1}{2r_d k_i},\tag{3.32}$$

that is, the attenuation length of the SAW in the solid divided by the lateral length of the drop. When $R = \mathcal{O}(1)$, acoustic radiation pressure should be considered to properly model the drop front, but when $R \ll 1$ (e.g. R = 1/5 as in our case), it can be neglected when modelling the drop front dynamics.

4. Theoretical results

In this section, we discuss the predictions of the model developed in § 3, and compare them with the experimental results. In § 4.1, we present results for a few chosen reference cases, and then we discuss the influence of model parameters, including the acoustic amplitude, A, the droplet volume V_d and the droplet kinematic viscosity v, on the results. In § 4.2 we discuss (approximate) travelling-wave solutions.

4.1. Main features of the results

In our simulations, we solve (3.29) numerically using COMSOLTM; see Appendix C for the description of the implementation. As the initial condition, we consider the two–dimensional parabolic drop of (dimensionless) cross-sectional area

$$\tilde{\mathcal{A}}_d = 2 \int_0^{\tilde{r}_d} \tilde{h}_d \left[1 - \left(\frac{\tilde{x}}{\tilde{r}_d} \right)^2 \right] d\tilde{x} = \frac{4}{3} \tilde{h}_d \tilde{r}_d, \tag{4.1}$$

(recall that tilded quantities are dimensionless) which remains constant during the drop evolution. The drop height parameter \tilde{h}_d is obtained from the known experimental (three-

dimensional) drop volume, $\mathcal{V}_d = \ell^3 \tilde{\mathcal{V}}_d$, as $\tilde{h}_d = 2 \tilde{\mathcal{V}}_d / (\pi \tilde{r}_d^2)$, using the formula for the volume $\tilde{\mathcal{V}}_d$ of a three-dimensional (3-D) parabolic cap of base radius \tilde{r}_d and height \tilde{h}_d . The 2-D parabolic initial condition is centred at $\tilde{x} = \tilde{x}_d$, and is written as

$$\tilde{h}(\tilde{x},0) = \begin{cases} \tilde{h}_p, & \tilde{x} < \tilde{x}_r(0), \\ (\tilde{h}_d - \tilde{h}_p) \left[1 - \left(\frac{\tilde{x} - \tilde{x}_d}{\tilde{r}_d} \right)^2 \right] + \tilde{h}_p, & \tilde{x}_r(0) \le \tilde{x} \le \tilde{x}_f(0), \\ \tilde{h}_p, & \tilde{x} > \tilde{x}_f(0), \end{cases}$$
(4.2)

where $\tilde{x}_r(0) = \tilde{x}_d - \tilde{r}_d$ and $\tilde{x}_f(0) = \tilde{x}_d + \tilde{r}_d$ are the initial positions of the rear and front contact lines of the drop, respectively (see figure 5). Here, \tilde{h}_p ($\ll \tilde{h}_d$) is the thickness of a precursor film, introduced to avoid the stress singularity associated with a moving contact line. It is well known (see, e.g. Diez & Kondic 2002), that the step size $\Delta \tilde{x}$ in the spatial discretisation should be similar to \tilde{h}_p to ensure numerical convergence, and therefore we use $\Delta \tilde{x} = \tilde{h}_p$ in our simulations. The specific value assigned to \tilde{h}_p has only a minor influence on the results; e.g. if \tilde{h}_p is doubled or halved, the change of spreading speed or drop height is just 1 %–2 %. All reported results are obtained using $\tilde{h}_p = 0.01$.

In implementing our model for the geometry defined above, we note that in the experiments, the SAW experiences minimal attenuation in regions of the actuator where fluid is not present, with significant attenuation only under the bulk droplet. To model this, we modify the factor ψ defined in (3.21), setting it to a constant value (no attenuation) in regions where the film height is smaller than some critical thickness \tilde{h}^* , with the exponential attenuation only where $\tilde{h} > \tilde{h}^*$, so that

$$\psi(\tilde{x}, \tilde{h}) = \begin{cases}
1, & \tilde{x} < \tilde{x}_{1}^{*}(\tilde{t}), \\
e^{-2\left[\tilde{k}_{s,i}(\tilde{x} - \tilde{x}_{1}^{*}(\tilde{t})) + \tilde{K}_{z}\left(\tilde{h} - \tilde{h}^{*}\right)\right]}, & \tilde{x}_{1}^{*}(\tilde{t}) \leq \tilde{x} \leq \tilde{x}_{2}^{*}(\tilde{t}), \\
e^{-2\tilde{k}_{s,i}\left[\tilde{x}_{2}^{*}(\tilde{t}) - \tilde{x}_{1}^{*}(\tilde{t})\right]}, & \tilde{x} > \tilde{x}_{2}^{*}(\tilde{t}),
\end{cases} (4.3)$$

where \tilde{x}_1^* , \tilde{x}_2^* are defined by $\tilde{h}(\tilde{x}_1^*, \tilde{t}) = \tilde{h}(\tilde{x}_2^*, \tilde{t}) = \tilde{h}^*$, and the SAW is assumed to propagate from $\tilde{x} < \tilde{x}_1^*(\tilde{t})$ in the direction of increasing \tilde{x} . In line with our discussion in § 3, in simulations we choose the cutoff film thickness \tilde{h}^* based on the thickness below which the bulk acoustic streaming becomes weak and mass transport is governed by other mechanisms (e.g. Rayleigh streaming and acoustic pressure Rezk *et al.* 2012, 2014), $\tilde{h}^* \approx (\lambda_{oil}/4)/\ell = 17 \, \mu \text{m}/\ell$.

We commence our analysis by considering the experimental case where an oil drop of volume 8 μ 1 is under the excitation of the 20 MHz SAW. Figure 6 shows the evolution of the thickness profile obtained by solving (3.29) for A = 1.44, 2, 6, 10 nm subject to the initial condition given by (4.2), and boundary conditions fixing the film thickness to h_p and requiring vanishing derivatives at the domain boundaries; the other parameter values are shown in table 2. For the low-amplitude cases (e.g. A < 2 nm, figures 6a and 6b), we see that capillary and gravitational forces dominate, leading to a continual spreading of the drop. The acoustic force is able to slightly drive the drop along the direction of propagation of the SAW, as is apparent by the movement of the two contact lines. In contrast, in the high-amplitude cases (e.g. A > 2 nm, figures 6c and 6d), the acoustic force plays a dominant role in governing the dynamics. We see that the evolution of the drop can be described by two regimes: an initial transient stage where the drop takes on a new shape, followed by a period of translation across the domain at near-constant speed, consistent with experimental results (see figure 3); as A increases, the duration of the transient stage

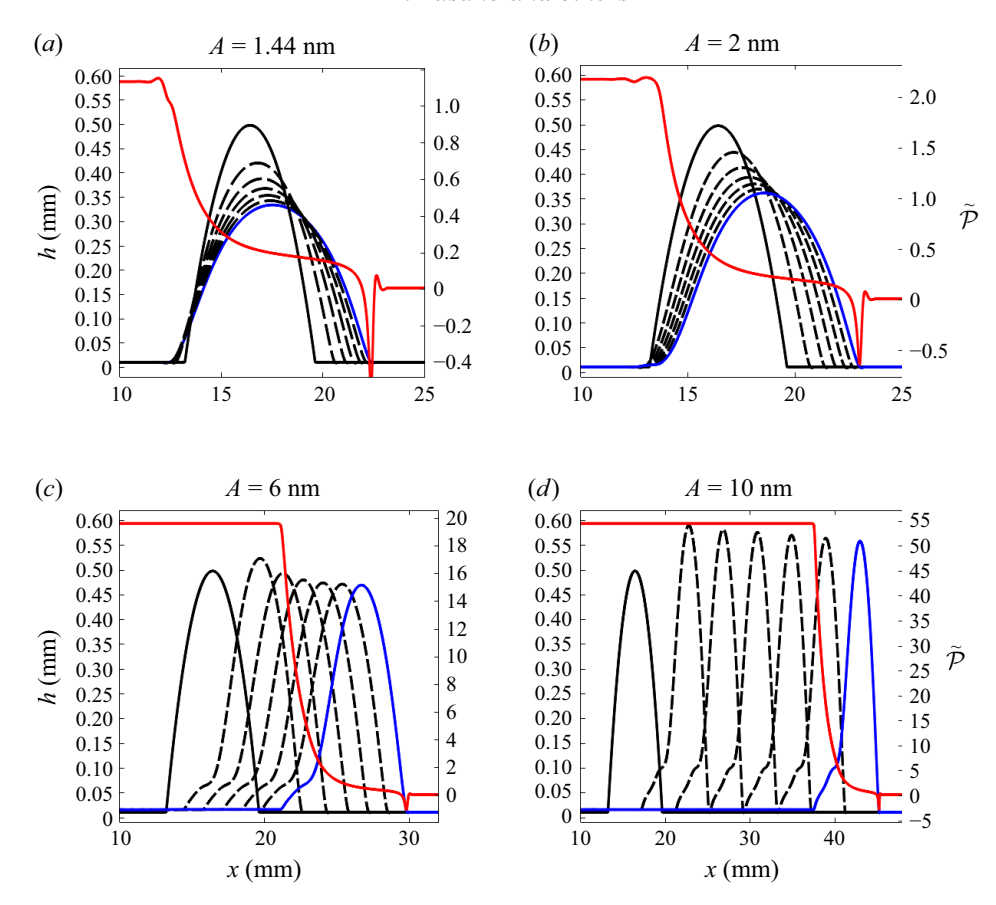


Figure 6. Evolution of thickness profile for different values of A. The black solid lines correspond to the initial condition, the dashed black lines to the profiles every time step $\Delta t = 1$ s and the solid blue line to t = 6 s. The red line stands for the effective dimensionless pressure $\tilde{\mathcal{P}}$ at t = 6 s. Note that the dip in the pressure curve corresponds to the dramatic change of curvature of the fluid interface at the front contact line.

decreases. The fluid region near the rear contact line, where the pressure gradient is largest, serves as a 'snow plough' that pushes the bulk drop along the direction of propagation of the SAW. The result is a near trave-ling-wave solution at long times, discussed further in § 4.2. The subtle, but continuous, decrease of the maximum height of the drop during this period is due to a thin trailing film (of approximate thickness h^*) that is left behind the bulk drop. We also note formation of a trailing foot forming spontaneously behind the main body of the drop for amplitudes A > 2 nm. This feature travels together with the main body of the droplet, in contrast to the trailing film, which stays behind. We direct the interested reader to the supplementary materials where animations for each of these four cases are shown (movie 4, movie 5, movie 6, movie 7).

Focusing next on the spreading speed, figure 7 plots the relative speed of spreading for both experiments and simulations. The numerical results (solid lines) show a monotonic increase in spreading speed as A increases, consistent with the experimental results (symbols). Note the distinct regimes in which the drops evolve, evident from the apparent change of slope of the curves, especially prominent in large-amplitude cases. Figure 7(b) shows the numerically calculated drop width, $w = x_2^* - x_1^*$, as a function of time, for different values of A. We once again emphasise the different behaviours exhibited by

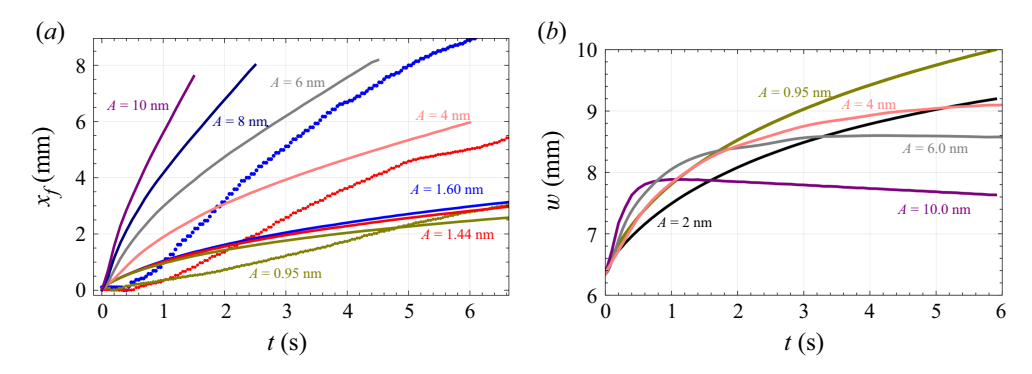


Figure 7. (a) Comparison between numerical (solid lines, amplitude values A as labelled, colour coded) and experimental results (solid dots, for measured amplitude values $A_n = 1.60$ nm (blue), 1.44 nm (red), 0.95 nm (olive)). (b) Numerically calculated drop width data plotted as a function of time for several A-values (colour matched with panel (a) where appropriate).

low- and high-amplitude solutions. For low-amplitude cases, the front contact line of the drop moves faster than the rear contact line, causing the drop to become thinner and wider. Conversely, for the high-amplitude cases, w initially increases and then remains nearly constant, or even decreases slowly.

Figure 7(a) illustrates a quantitative difference between experiment and simulations: assuming that $A = A_n$ (see also the relevant discussion in § 3), the simulated drops travel at a slower pace. While it is not yet clear why this difference arises, some plausible reasons, in addition to possible differences between A and A_n (Royer & Dieulesaint 1996), include: (i) the potential relevance of inertial effects that are not included in the model at order M_a (the solution v_1) (Zarembo 1971; Orosco & Friend 2022; Dubrovski, Friend & Manor 2023); (ii) the omission of contributions from the boundary layer flow near the solid surface, i.e. the Rayleigh law of streaming; (iii) the capillary waves that appear at the free surface of the film (Lighthill 1978; Morozov & Manor 2017); (iv) the use of a 2-D model to understand a 3-D system; and (v) the neglect of the ultrasonic wave reflection off the free surface of the liquid. We have verified that the numerical results are independent of the precise values assigned to h^* and h_p , suggesting that neither boundary layer thickness nor precursor thickness are relevant here. We have also carried out some preliminary simulations of a 3-D oil drop, which suggest that the 2-D model used in the present work is not responsible for the quantitative differences between experiments and simulations (we leave the discussion of 3-D effects for future work). Clearly, more work will be needed to uncover the sources of the quantitative differences between experiments and simulations.

To summarise the numerical results presented so far, figure 8 plots the numerically predicted values of the front speed, v_f , the maximum drop height, h_{max} and the drop width, w, all calculated at t=9 s, as a function of SAW amplitude A. This figure illustrates the transition between the two types of dynamics observed: for low and moderate A-values ($A \le 2$ nm) we observe near-symmetric drop spreading due primarily to capillary forces, however, for large values (A > 2 nm) the front speed increases approximately quadratically as A increases, while the maximum height/width of the drop increases/decreases approximately linearly with respect to the amplitude value.

Before concluding this section, we briefly discuss how the results depend on the oil viscosity. We have also carried out simulations using different drop volumes; while the results are consistent with the experimental ones, shown in figure 4(b), the influence of the change of fluid volume is, however, weaker than in the experiments (the results not shown for brevity). When varying the kinematic viscosity, ν (assuming $\nu' = \nu$), without

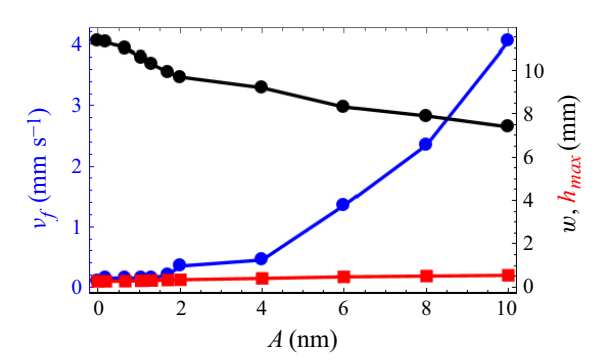


Figure 8. Long time (calculated at t = 9 s) values of the front speed, v_f (in mm s⁻¹, blue filled circles), maximum thickness, h_{max} (mm, red filled squares) and drop width, w (cm, black filled circles), as functions of A. Note that v_f is plotted using the left y-axis while w and h_{max} are plotted using the right y-axis. The points correspond to the raw data, and the solid lines connecting them guide the eye.

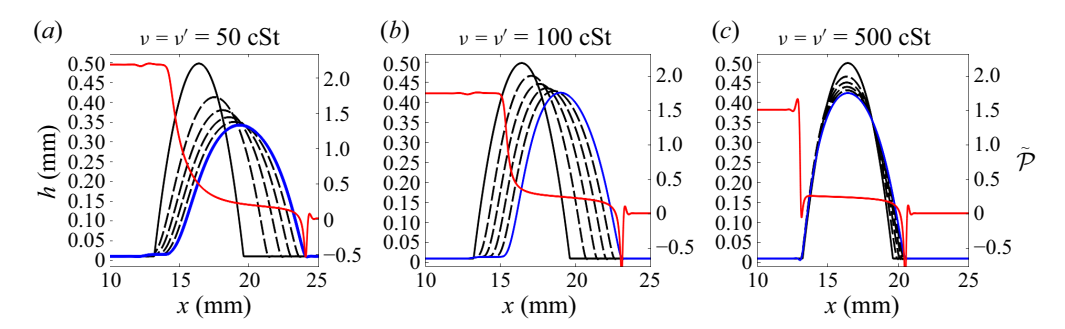


Figure 9. Evolution of thickness profile for A=2 nm for drops of different viscosities, $\nu=\nu'=50$, 100, 500 cSt, indicated in each panel. The black solid lines correspond to the initial condition, the dashed black lines to the profiles every time step $\Delta t=2$ s and the solid blue line to t=10 s. The red line denotes the effective dimensionless pressure $\tilde{\mathcal{P}}$ at t=10 s.

acoustic forcing (A=0), viscosity only (linearly) affects the time scale. With acoustics, however, the dynamics changes in a nonlinear fashion, see figure 9. The mechanism behind this nonlinear dependence is traced to the prefactor of the non-conservative term in (3.29), which decreases as \tilde{K}_z (defined in (A6)) grows and $\tilde{\mathcal{C}}$ (defined in (3.23)) decreases in magnitude, yielding a relatively large attenuation length. This substantially weakens the forcing at the front, while nearly balancing gravitational and capillary forces at the rear, effectively stalling the drop motion for large viscosity values, in qualitative agreement with the experimental findings of figure 4(a).

4.2. Travelling-wave solution

In view of the results presented so far, we now briefly explore a possible trave-ling-wave solution of (3.29) which appears present for sufficiently large SAW amplitudes, such as the case shown in figures 6(c) and 6(d).

Within this framework, we assume that the whole drop translates with constant speed \tilde{U} , so that

$$\tilde{x}_r(\tilde{t}) = \tilde{U}\tilde{t}, \quad \tilde{x}_f(\tilde{t}) = \tilde{w} + \tilde{U}\tilde{t},$$
(4.4)

where (constant) $\tilde{\mathbf{w}}$ is the width of the moving drop. Here, we will consider that the rear (front) contact lines of the travelling drop are given by \tilde{x}_1^* (\tilde{x}_2^*) (see figure 5), since the

SAW force that drives it is felt only where $\tilde{h} > \tilde{h}^*$. Then, we define $\tilde{\xi} = \tilde{x} - \tilde{x}_1^*(\tilde{t}) = \tilde{x} - \tilde{U}\tilde{t}$ and assume that $\tilde{h}(\tilde{x},\tilde{t}) = \tilde{h}(\tilde{\xi})$, so that (3.29) becomes (see also Buckingham, Shearer & Bertozzi 2003; Perazzo & Gratton 2004; Giacomelli, Gnann & Otto 2016 for similar studies without SAW forces)

$$\tilde{U}\frac{\mathrm{d}\tilde{h}}{\mathrm{d}\tilde{\xi}} + \frac{\mathrm{d}}{\mathrm{d}\tilde{\xi}} \left[\tilde{h}^{3} \frac{d}{\mathrm{d}\tilde{\xi}} \left(-\frac{\mathrm{d}^{2}\tilde{h}}{\mathrm{d}\tilde{\xi}^{2}} + Bo\,\tilde{h} + \frac{\mathcal{S}\tilde{C}_{z}}{2\tilde{K}_{z}} \psi(\tilde{\xi},\tilde{h}) \right) + \tilde{\mathcal{C}}\frac{3\mathcal{S}}{8\tilde{K}_{z}^{4}} \psi(\tilde{\xi},\tilde{h}) \left(2\tilde{K}_{z}^{2}\tilde{h}^{2} - 1 + e^{2\tilde{K}_{z}\tilde{h}} (1 - 2\tilde{K}_{z}\tilde{h}) \right) \right] = 0,$$
(4.5)

where

$$\psi(\tilde{\xi}, \tilde{h}) = e^{-2[\tilde{k}_{s,i}\tilde{\xi} + \tilde{K}_z(\tilde{h} - \tilde{h}^*)]}.$$
(4.6)

This equation can be integrated once to yield

$$\tilde{U}\tilde{h} + \tilde{h}^{3} \frac{\mathrm{d}}{\mathrm{d}\tilde{\xi}} \left[-\frac{\mathrm{d}^{2}\tilde{h}}{\mathrm{d}\tilde{\xi}^{2}} + Bo \ \tilde{h} + \frac{\mathcal{S}\tilde{C}_{z}}{2\tilde{K}_{z}} \psi(\tilde{\xi}, \tilde{h}) \right]
+ \tilde{C} \frac{3\mathcal{S}}{8\tilde{K}_{z}^{4}} \psi(\tilde{\xi}, \tilde{h}) \left(2\tilde{K}_{z}^{2}\tilde{h}^{2} - 1 + e^{2\tilde{K}_{z}\tilde{h}} (1 - 2\tilde{K}_{z}\tilde{h}) \right) = \tilde{J},$$
(4.7)

where \tilde{J} represents the flux. The travelling-wave solution must be calculated for $0 \leq \tilde{\xi} \leq \tilde{w}$, along with the following boundary conditions at $\tilde{\xi} = 0$:

$$\tilde{h}(0) = \tilde{h}^*, \quad \tilde{h}'(0) = \tilde{h}'''(0) = 0,$$
(4.8)

where the prime denotes $d/d\tilde{\xi}$. The values of $\tilde{h}''(0)$, \tilde{U} and \tilde{w} are determined by

$$\tilde{h}(\tilde{w}) = \tilde{h}^*, \quad \tilde{J}(0) = \tilde{J}(\tilde{w}), \quad \tilde{A}_d = \int_0^{\tilde{w}} \tilde{h}(\tilde{\xi}) \,\mathrm{d}\tilde{\xi}.$$
 (4.9)

Note that \tilde{J} corresponds to the flux within a thin film of thickness \tilde{h}^* that enters the drop at \tilde{w} and comes out of it at $\tilde{\xi} = 0$ (with respect to the reference frame fixed at the drop).

We developed an iterative scheme to perform the numerical integration of (4.7), under the conditions given by (4.9). We start by guessing values of $\tilde{h}''(0)$, \tilde{U} and $\tilde{\xi}_f$ to perform the integration of (4.7) and modify them accordingly until these conditions are satisfied within a small relative error (typically, 10^{-7} or even smaller). After obtaining convergence for a given \tilde{A} , we use these converged values of $\tilde{h}''(0)$, \tilde{U} and $\tilde{\xi}_f$ as new guess values for $\tilde{A} + \Delta \tilde{A}$ (numerical continuation; $\Delta \tilde{A}$ has to be very small to reach convergence).

Figure 10(a) shows the dimensional drop profiles for the values of A considered so far. Clearly, drops become taller and narrower as A increases. Figure 10(b) shows the dependence of drop speed, v_f , its width, w, and the maximum thickness, h_{max} , on A. Note that this simplified model predicts that the speed depends approximately quadratically on the amplitude, A, while the maximum height of the drop depends approximately linearly on A, as was found in the full numerics (see figure 8b).

This approximate formulation shows that the simple travelling-wave solution can capture, at least qualitatively, certain features of the experimental and numerical drops. Clearly, this description cannot account for the rear region of the drop (see figures 6 and 10a) because the values of h' and h''' at the left contact line cannot be determined a priori, and both have been set to zero (for lack of better choice) in the travelling-wave calculations.

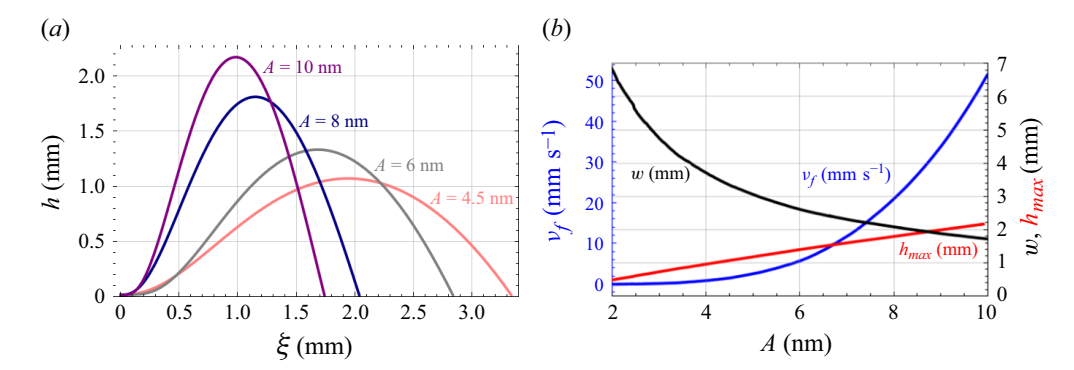


Figure 10. (a) Thickness profile of the travelling-wave solution for: A = 4.5 nm, 6 nm, 8 nm, 10 nm. (b) Front speed, v_f (mm s⁻¹, blue line), drop width, w (mm, black line) and maximum height, h_{max} (mm, red line), of the travelling drop as a function of A; front speed is plotted on the left y-axis while drop width and maximum height are on the right y-axis.

5. Conclusions

In this work, we consider the problem of a spreading silicone oil drop driven by a SAW propagating in the supporting substrate. Our particular focus is on a theoretical framework that describes drops of millimetric thickness, for which the main driving mechanism is the Eckart streaming. Therefore, we focus on a different regime from that relevant for the much thinner drops considered by Rezk *et al.* (2012, 2014), for which Schlichting and Rayleigh streaming effects are dominant. To the best of our knowledge, modelling the dynamics of millimetric drops under the action of SAW and capillary stresses has not been considered so far in the literature. We also present selected experimental results for the qualitative validation of our model.

While developing our theoretical description of drop spreading, it became apparent that an important effect, which requires careful modelling, involves the attenuation of the SAW under the evolving drop. The model we derived, assuming the thin film limit and implementing the long-wave approximation, shows that the oil drop is essentially pushed by the SAW forcing from behind. For the highly viscous oils considered in our experiments, the effective SAW forcing is due to both viscous dissipation, and to spatial variation of the leaked acoustic wave in the fluid due to SAW attenuation in the solid. A consequence of the driving mechanism is that the dynamics itself is substantially different from the familiar case of drops driven by gravity, where the volume force is a constant and not rapidly decreasing along the drop, as occurs with the SAW force. In particular, we find that the drops tend to keep almost the same shape as time and spreading progress, and also that they reach essentially constant spreading speeds at long times. This contrasts with the gravity-driven case, where the spreading speed decreases due to drop thinning.

While not all details of the experimental results are fully understood, in general, we find reasonable agreement between the experimental and theoretical results, further supporting the basic premises underlying the developed acousto-fluidic model. In particular, our model provides good qualitative predictions for drop shapes, spreading speeds and the dependence of the results on the SAW displacement amplitude at the solid surface (the SAW intensity). Both theoretical and experimental results show asymmetric drop shapes with a thin trailing film left behind, and both appear to reach a constant spreading speed asymptotically in time. The latter finding motivated us to formulate a simplified travelling-wave model. The resulting analytical solution predicts an approximately linear increase in the drop thickness and a quadratic increase of the spreading speed with the acoustic

intensity (SAW normal displacement amplitude at the solid surface), A. Such predicted trends are consistent with those of the full theoretical model and the experiments.

While many features of the experimental results have been rationalised using our theoretical models and simulations, much remains to be done. Further investigation is required to shed light on the features of dynamic drop profiles under SAW excitation. The transition from a 3-D to a quasi-2-D dynamics is also intriguing: under strong SAW excitation, a drop spreads primarily along the path of the SAW and may be described to leading order using the 2-D model given here. However, at weak SAW excitation, where the drop also spreads radially due to the relaxation of capillary stress at the free drop surface, the drop dynamics is inherently of the 3-D type. Hence, 3-D aspects of the drop dynamics, in particular in cases where the contributions to flow from capillary and SAW stresses are comparable, remain to be simulated and understood.

Supplementary movies. Supplementary movies are available at https://doi.org/10.1017/jfm.2025.10802.

Acknowledgements. This work was supported by the donors of ACS Petroleum Research Fund under PRF# 62062-ND9 and by BSF grant No. 2020174. J.A.D. acknowledges support from Consejo Nacional de Investigaciones Científicas y Técnicas (CONICET, Argentina) with Grant PIP 02114-CO/2021 and Agencia Nacional de Promoción Científica y Tecnológica (ANPCyT, Argentina) with Grant PICT 02119/2020.

Declaration of interests. The authors report no conflict of interest.

Appendix A. First-order velocity components and SAW force

As mentioned in the main text, although we deal with imaginary equations in the model derivation, it is understood that the real part of these complex equations is taken as the result for physically relevant real quantities. This includes the first-order velocity field, v_1 , given by (3.14), and the acoustic force on the induced steady streaming flow, F_s , given by (3.17), which we now discuss in detail.

We first examine v_1 whose real parts in two dimensions can be written as

$$v_{1,x} = V_x A \omega e^{-k_{s,i}x - K_z z},$$

 $v_{1,z} = V_z A \omega e^{-k_{s,i}x - K_z z},$ (A1)

where the factors V_x and V_z are

$$V_{x} = \frac{1}{\Delta} \left[k_{s,i} \cos \left(\frac{\theta}{2} + k_{s,r} x + z \Delta \sin \left(\frac{\theta}{2} \right) - \omega t \right) + k_{s,r} \sin \left(\frac{\theta}{2} + k_{s,r} x + z \Delta \sin \left(\frac{\theta}{2} \right) - \omega t \right) \right], \tag{A2}$$

$$V_z = \cos\left(k_{s,r}x + z\Delta\sin\left(\frac{\theta}{2}\right) - \omega t\right),\tag{A3}$$

with

$$\Delta = \sqrt{\left|\kappa_s^2 - \kappa^2\right|} = \sqrt[4]{\left(k_{s,i}^2 - k_{s,r}^2 + k_r^2 - k_i^2\right)^2 + (2k_{s,i}k_{s,r} - 2k_ik_r)^2},\tag{A4}$$

$$\theta = \arg\left(\kappa_s^2 - \kappa^2\right),\tag{A5}$$

$$K_z = \Delta \cos \left(\theta/2\right). \tag{A6}$$

Turning next to F_s , in order to find the real part we substitute (A1) with the subsequently defined parameters into (3.17), and find explicit expressions for the acoustic force components in the form

$$F_{s,x} = C_x P_0 e^{-2(k_{s,i}x + K_z z)}, (A7)$$

$$F_{s,z} = C_z P_0 e^{-2(k_{s,i}x + K_z z)}, (A8)$$

where P_0 is defined in (3.21), and

$$C_x = \frac{k_{s,i}k_{s,r}^2 + \Delta\cos\left(\frac{\theta}{2}\right)k_{s,i}K_z + k_{s,i}^3 + \Delta\sin\left(\frac{\theta}{2}\right)k_{s,r}K_z}{\Delta^2},$$
 (A9)

$$C_z = \frac{\cos\left(\frac{\theta}{2}\right)k_{s,i}^2 + \sin\left(\frac{\theta}{2}\right)k_{s,i}k_{s,r} + \Delta K_z}{\Delta}.$$
(A10)

We point out that F_s is a non-conservative force; it cannot be written as the gradient of a potential, except for a special choice of parameter values that satisfy $k_{s,i}C_z = K_zC_x$ (see (A7) and (A8)).

Appendix B. Approximate solution of the SAW force

In this section, we discuss an approximate solution for the SAW force in certain contexts. Section B.1 discusses simplifications to the model considered in Appendix A, using the appropriate parameters for Polydimethylsiloxane (PDMS), as considered in the experiments and in the main body of the paper. To illustrate the differences that occur in the case of less viscous fluid (water), in § B.2 we discuss appropriate simplifications for such cases. Finally, in § B.3 we discuss the model that results if viscous losses are neglected, and the relation of the obtained model to that proposed decades ago by Shiokawa, Matsui & Ueda (1990).

In this section, we take a closer look at the acoustic force F_s , given by (3.17), on the induced steady streaming flow. We first note that, for our parameter values, we can define the small quantities

$$\varepsilon_s = \frac{k_{s,i}}{k_{s,r}}$$
 and $\varepsilon = \frac{k_i}{k_r} \approx \frac{\beta}{2}$. (B1)

These two parameters ε_s and ε are always small, and of the same order of magnitude, for the PDMS used here (see (3.12) and the surrounding discussion). To approximate the SAW force, we can expand the auxiliary variables and SAW force coefficients, given in (A4), (A5), (A6), (A9) and (A10), in terms of ε_s and ε . Retaining only linear terms in the expansions (neglecting any terms quadratic in ε_s , ε that are of higher order than those retained) yields the following expressions:

$$\Delta \approx k_{s,r}\alpha_{1},$$

$$\theta \approx \pi - \frac{2}{\alpha_{1}^{2}}(1 + \alpha_{1}^{2})\varepsilon + \frac{2}{\alpha_{1}^{2}}\varepsilon_{s},$$

$$K_{z} \approx \frac{k_{s,r}}{\alpha_{1}}(1 + \alpha_{1}^{2})\varepsilon - \frac{k_{s,r}}{\alpha_{1}}\varepsilon_{s},$$

$$C_{x} \approx \frac{k_{s,r}(1 + \alpha_{1}^{2})}{\alpha_{1}^{2}}\varepsilon,$$

$$C_{z} \approx \alpha_{1}C_{x},$$
(B2)

where we have simplified the expressions by defining

$$\alpha_1 = \sqrt{\frac{k^2}{k_{s,r}^2} - 1} = \sqrt{\frac{c_s^2}{c^2} - 1},$$
(B3)

since $k_{s,r} = \omega/c_s$. This coefficient yields the Rayleigh angle θ_R as: $\tan \theta_R = 1/\alpha_1$. From the outlined approximation, we obtain that the resultant force is given by

$$F_{s,x} \approx \frac{\rho_0 A^2 \omega^2 (1 + \alpha_1)^2 k_{s,r}}{\alpha_1^2} \varepsilon \ e^{-2(k_{s,i}x + K_z z)},$$
 (B4)

$$F_{s,z} \approx \alpha_1 F_{s,x}$$
. (B5)

The approximations made in (B2) lead to an attenuation factor K_z that is approximately 12% smaller and force coefficients C_x and C_z that are approximately 2% bigger and 6% smaller, respectively, with respect to the quantities in the exact expressions given in (A6), (A9), and (A10). Note that the approximate force components obtained in (B4), (B5) (also) do not yield a conservative force, since $K_z \neq \alpha_1 k_{s,i}$.

B.2. Water

Next, we consider modelling a lower viscosity fluid such as water, characterised by a similar density and phase velocity to oil (PDMS) so that the imaginary component of the wavenumber in the solid is similar (see (3.11)). However, the large decrease in viscosity in the case of water leads to a much reduced value of the imaginary wavenumber in the liquid, k_i (see (3.7)). Thus for water, our assumption that ε and ε_s are of the same order of magnitude fails; in fact, here we have $\varepsilon_s^2 \sim \varepsilon$ so that we need to also retain terms that are quadratic in ε_s ; the next largest terms in the expansion are those proportional to ε_s^3 which we also include for the purpose of comparison with the approximation in the case of neglecting viscous dissipation which is discussed later in § B.3. Note that we neglect any cross-terms that may appear in the expansions as they are higher order than the terms retained.

Performing an asymptotic expansion of the auxiliary variables and SAW force coefficients appropriate for the water leads to the following approximate expressions:

$$\Delta \approx k_{s,r}\alpha_{1} + \varepsilon_{s}^{2} \left(\frac{k_{s,r}}{\alpha_{1}^{3}} + \frac{k_{s,r}}{2\alpha_{1}}\right),$$

$$\theta \approx -\pi + \frac{2}{\alpha_{1}^{2}}\varepsilon_{s} - \frac{2\left(1 + \alpha_{1}^{2}\right)}{\alpha_{1}^{2}}\varepsilon,$$

$$K_{z} \approx \frac{k_{s,r}}{\alpha_{1}}\varepsilon_{s} - \frac{k_{s,r}\left(1 + \alpha_{1}^{2}\right)}{\alpha_{1}}\varepsilon,$$

$$C_{x} \approx \frac{k_{s,r}\left(1 + \alpha_{1}^{2}\right)}{\alpha_{1}^{2}} \left(\varepsilon + \frac{\varepsilon_{s}^{3}}{\alpha_{1}^{2}}\right),$$

$$C_{z} \approx \frac{k_{s,r}\left(1 + \alpha_{1}^{2}\right)}{\alpha_{1}} \left(-\varepsilon + \frac{\varepsilon_{s}^{3}}{\alpha_{1}^{4}}\right).$$
(B6)

We pause to discuss the difference between the approximated complex arguments in the case of oil and water. Note that the two expressions for θ ((B2) and (B6)) have the same first-order correction terms with respect to the small parameters ε and ε_s ; however, the sign of the sum of these two terms is opposite for the case of PDMS (negative) and

water (positive) – which is due to the much reduced value of the imaginary wavenumber in the liquid, k_i , in the case of water as compared with PDMS (see (3.6) and (3.8)). The result of this sign change has the effect of moving the complex argument from quadrant II (in the case of PDMS) to quadrant III (in the case of water); as a result, the approximation for the sine function in the SAW force coefficients changes sign and thus the overall value of the SAW force coefficients is much reduced (see (A9) and (A10)).

From the approximation in (B6), we can see that the resultant force for water, at leading order, is given by

$$F_{s,x} \approx \frac{\rho_0 A^2 \omega^2 (1 + \alpha_1)^2 k_{s,r}}{\alpha_1^2} \varepsilon e^{-2(k_{s,i}x + K_z z)}, \tag{B7}$$

$$F_{s,z} \approx -\alpha_1 F_{s,x}$$
. (B8)

Using appropriate parameter values for water, we find that the SAW force for water, (B7) and (B8), has a coefficient that is approximately two orders of magnitude smaller than that for PDMS, see (B4) and (B5) (due to the fact that ε is much smaller for water than oil). Additionally, the z component of the SAW force has a negative prefactor, C_z .

Before closing this discussion, we note that if one wants to accurately study the dynamics of water drops in the present context, one must also include a disjoining pressure term in (3.27) to account for the partial wettability of the fluid.

B.3. Neglecting viscous dissipation

We now discuss briefly a modified model obtained if viscous dissipation is neglected by setting $k_i = 0$, which is akin to the approach presented by Shiokawa *et al.* (1989, 1990). To do this, the simplest approach is to set $k_i = 0$ in the exact formulae ((A4), (A5), (A6), (A9), and (A10)) and then re-expand the quantities in terms of the remaining small parameter ε . Doing this, one finds that the auxiliary variables and the SAW force coefficients are now given by

$$\Delta \approx k_{s,r}\alpha_{1},$$

$$\theta \approx -\pi + \frac{2}{\alpha_{1}^{2}}\varepsilon_{s},$$

$$K_{z} \approx \frac{k_{s,r}}{\alpha_{1}}\varepsilon_{s},$$

$$C_{x} \approx \frac{k_{s,r}\left(1 + \alpha_{1}^{2}\right)}{\alpha_{1}^{4}}\varepsilon_{s}^{3},$$

$$C_{z} \approx \frac{1}{\alpha_{1}}C_{x}.$$
(B9)

We note that this approximation is exactly what is found by simply setting $\varepsilon = 0$ in the approximation for the case of a low viscosity fluid such as water (see (B6)). Hence, if viscous dissipation is neglected, the SAW force is given as

$$F_{s,x} \approx \frac{\rho A^2 \omega^2 \left(1 + \alpha_1^2\right)}{\alpha_1^4} k_{s,r} \varepsilon_s^3 e^{-2k_{s,i}(x + \frac{1}{\alpha_1} z)}, \tag{B10}$$

$$F_{s,z} \approx \frac{1}{\alpha_1} F_{s,x},$$
 (B11)

which can be rewritten in terms of a potential ϕ_s , so that $F_s = -\nabla \phi_s$ is a conservative volume force with

$$\phi_{s} = \frac{\rho A^{2} \omega^{2} \left(1 + \alpha_{1}^{2}\right)}{2\alpha_{1}^{4}} \varepsilon_{s}^{2} e^{-2k_{s,i}(x + \frac{1}{\alpha_{1}}z)}.$$
(B12)

We note that without viscous dissipation, the force components are five orders of magnitude smaller than when the viscosity is considered, compare for example (A9), (A10) to (B9) with the given parameter values. As a result, the force in (B10) and (B11) has no effect on drop dynamics on the time scales investigated. Such a finding inspires comparison with the results presented in Shiokawa *et al.* (1989, 1990), and given in terms of our variables as

$$\phi_{\text{shio}} = \frac{1 + \alpha_1^2}{2} \rho A^2 \omega^2 e^{-2k_{s,i}(x + \alpha_1 z)}.$$
 (B13)

Note that, for the considered parameter values, this expression leads to a force that is approximately three orders of magnitude larger compared with what is found from our model, i.e. (B12). Further, our model predicts a different attenuation factor in z as well as a different force prefactor than what is found in Shiokawa *et al.* (1989, 1990). In those works, the authors find that $K_z = \alpha_1 k_{s,i}$, as opposed to our model which yields $K_z \approx k_{s,r} \varepsilon_s / \alpha_1 = k_{s,i}/\alpha_1$. From the physical point of view, one expects larger viscous dissipation at a given z (distance from the substrate, into the liquid), when the Rayleigh angle, θ_R , increases and tends to $\pi/2$ (see figure 5, where the angle is measured clockwise from the normal to the substrate). This is because the leaky wave travels a longer distance along the ray (for given z) for larger θ_R , and thus its amplitude is more attenuated. For example, if $z \to z_s$, we have $z \to \pi/2$ and $z \to \pi/2$ and $z \to \pi/2$ and $z \to \pi/2$, we have $z \to \pi/2$ and then one expects $z \to \pi/2$, we have $z \to \pi/2$ and then one expects $z \to \pi/2$, we have $z \to \pi/2$, and then one expects $z \to \pi/2$, and not $z \to \pi/2$, we have $z \to \pi/2$, and then one expects $z \to \pi/2$.

Appendix C. Computational implementation

Equation (3.29) is written in a form convenient for the use of COMSOLTMMultiphysics PDE Coefficients Form. This package solves, by finite elements, a vectorial equation for the unknown vector $\mathbf{u} = (u_1, u_2, \dots, u_N)^{\mathsf{T}}$. The equation is of the form

$$e^{\frac{\partial^2 u}{\partial t^2}} + d^{\frac{\partial u}{\partial t}} + \nabla \cdot (-c\nabla u - \alpha u + \gamma) + \beta \nabla u + a u = f,$$
 (C1)

where the coefficients of the N scalar equations are in the matrices e, d, γ , a (of dimensions $N \times N$), α , β (of dimensions $N \times N \times n$), c (of dimensions $N \times N \times n \times n$) and the vector f (of dimension N), where n is the spatial dimension of the problem (n = 1, 2, 3). In index notation, this equation reads as

$$e_{ij}\frac{\partial^{2}u_{j}}{\partial\tilde{t}^{2}} + d_{ij}\frac{\partial u_{j}}{\partial\tilde{t}} + \frac{\partial}{\partial\tilde{x}_{l}}\left(-c_{ijkl}\frac{\partial u_{j}}{\partial\tilde{x}_{k}} - \alpha_{ijl}u_{j} + \gamma_{il}\right) + \beta_{ijl}\frac{\partial u_{j}}{\partial\tilde{x}_{l}} + a_{ij}u_{j} = f_{i}, \quad (C2)$$

where i, j = 1, ..., N and k, l = 1, ..., n.

The considered system, given by (3.29), contains two components $u = (\tilde{h}, \tilde{\mathcal{P}})$ (N = 2) and we use two equations, namely, (3.29) and (3.30) for (n = 1), corresponding to the solution depending on a single spatial variable, \tilde{x} .

In the following, we list the non-vanishing coefficients (we omit the indices k and l for brevity and consider $\tilde{x}_1 \equiv \tilde{x}$ since k = l = 1):

(i) Row 1 (i = 1) for (3.29)

$$d_{11} = 1, \quad c_{12} = \tilde{h}^3, \quad \gamma_1 = -\tilde{\mathcal{C}} \frac{3S}{8\tilde{K}_z^4} \psi(\tilde{x}, \tilde{h}) \left(2\tilde{K}_z^2 \tilde{h}^2 - 1 + e^{2\tilde{K}_z \tilde{h}} (1 - 2\tilde{K}_z \tilde{h}) \right) \right]$$
(C3)

(ii) Row 2 (i = 2) for (3.30)

$$c_{21} = -1, \quad a_{21} = -Bo, \quad a_{22} = 1, \quad f_2 = \frac{S\tilde{C}_z}{2\tilde{K}_z}\psi(\tilde{x}, \tilde{h})$$
 (C4)

At the domain ends, we apply Dirichlet boundary conditions $\tilde{h} = \tilde{h}_p$, where \tilde{h}_p is the precursor film thickness, and $\partial \tilde{h}/\partial \tilde{x} = 0$. In order to achieve convergent numerical simulations, we discretise the domain using $\Delta \tilde{x} = \tilde{h}_p$.

REFERENCES

ALTSHULER, G. & MANOR, O. 2015 Spreading dynamics of a partially wetting water film atop a MHz substrate vibration. *Phys. Fluids* 27, 102103.

ALZUAGA, S., MANCEAU, J.F. & BASTIEN, F. 2005 Motion of droplets on solid surface using acoustic radiation pressure. J. Sound Vib. 282, 151–162.

AMON, C.H., MURTHY, J., YAO, S.C., NARUMANCHI, S., WU, C.F. & HSIEH, C.C. 2001 MEMS-enabled thermal management of high-heat-flux devices EDIFICE: embedded droplet impingement for integrated cooling of electronics. *Exp. Therm. Fluid Sci.* 25, 231–242.

ARZT, R.M., SALZMANN, E. & DRANSFELD, K. 1967 Elastic surface waves in quartz at 316 MHz. Appl. Phys. Lett. 10, 165–167.

ATENCIA, J. & BEEBE, D.J. 2005 Controlled microfluidic interfaces. Nature 437, 648-655.

BALLANTINE, D.S., WHITE, R.M., MARTIN, S.J., RICCO, A.J., ZELLERS, E.T., FRYE, G.C. & WOHLTJEN, H. 1996 Acoustic Wave Sensors: Theory, Design and Physico-Chemical Applications. Elsevier.

BAR-COHEN, A., ARIK, M. & OHADI, M. 2006 Direct liquid cooling of high flux micro and nano electronic components. *Proc. IEEE* **94**, 1549–1570.

BIWERSI, S., MANCEAU, J.F. & BASTIEN, F. 2000 Displacement of droplets and deformation of thin liquid layers using flexural vibrations of structures. Influence of acoustic radiation pressure. *J. Acoust. Soc. Am.* **107**, 661–664.

BORGNIS, F.E. 2010 Acoustic radiation pressure of plane compressional waves. *Rev. Mod. Phys.* **25**, 653–664. BROWN, D. & COX, A.J. 2009 Innovative uses of video analysis. *Phys. Teacher* **47**, 145–150.

Brunet, P., Baudoin, M., Matar, O.Bou & Zoueshtiagh, F. 2010 Droplet displacements and oscillations induced by ultrasonic surface acoustic waves: a quantitative study. *Phys. Rev. E* 81, 036315.

Brunet, P., Eggers, J. & Deegan, R.D. 2007 Vibration-induced climbing of drops. *Phys. Rev. Lett.* 99, 144501.

BRUNET, P., EGGERS, J. & DEEGAN, R.D. 2009 Motion of a drop driven by substrate vibrations. *Eur. Phys. J. Special Topics* **166**, 11.

BUCKINGHAM, R., SHEARER, M. & BERTOZZI, A. 2003 Thin film traveling waves and the Navier slip condition. SIAM J. Appl. Maths 63, 722–744.

CAMPBELL, J.J. 1970 Propagation of surface waves at the boundary between a piezoelectric crystal and a fluid medium. *IEEE Trans. Sonics Ultrason.* 17, 71–76.

CAMPBELL, J.J. & JONES, W.R. 1968 A method for estimating optimal crystal cuts and propagation directions for excitation of piezoelectric surface waves. *IEEE Trans. Sonics Ultrason.* 15, 209–217.

CAMPBELL, J.J. & JONES, W.R. 1970 Propagation of surface waves at the boundary between a piezoelectric crystal and a fluid medium. *IEEE Trans. Son. Ultrason.* 17, 71–76.

CHU, B.T. & APFEL, R.E. 1982 Acoustic radiation pressure produced by a beam of sound. *J. Acoust. Soc. Am.* 72, 1673–1687.

72, 16/3–168/.
CRASTER, R.V. & MATAR, O.K. 2009 Dynamics and stability of thin liquid films. Rev. Mod. Phys. 81,

1131–1198.
DIEZ, J.A. & KONDIC, L. 2002 Computing three-dimensional thin film flows including contact lines.
J. Comput. Phys. 183, 274–306.

DUBROVSKI, O., FRIEND, J. & MANOR, O. 2023 Theory of acoustic streaming for arbitrary Reynolds number flow. *J. Fluid Mech.* **975**, A4.

- DUSSAN, E.B. & CHOW, R.T.P. 1983 On the ability of drops or bubbles to stick to non-horizontal surfaces of solids. J. Fluid Mech. 137, 1–29.
- DUSSAN V., E.B. & DAVIS, S.H. 1974 On the motion of a fluid-fluid interface along a solid surface. J. Fluid Mech. 65, 71–95.
- ECKART, C. 1948 Vortices and streams caused by sound waves. Phys. Rev. 73, 68-76.
- FASANO, M., DIEZ, J.A., MANOR, O., KONDIC, L. & CUMMINGS, L. 2025 Phase separation of a binary fluid mixture under external forcing. *J. Engng Maths* 152, 12.
- FENDLER, J.H. 1996 Self assembled nanostructured materials. Chem. Mater. 8, 1616–1624.
- FLETCHER, L.S., SERNAS, V. & GALOWIN, L.S. 1974 Evaporation from thin water films on horizontal tubes. *Ind. Engng Chem. Process Des. Dev.* 13, 265–269.
- GIACOMELLI, L., GNANN, M. & OTTO, F. 2016 Rigorous asymptotics of traveling-wave solutions to the thin-film equation and Tanner's law. *Nonlinearity* 29, 2497–2536.
- GUTTENBERG, Z.V., RATHGEBER, A., KELLER, S., RÄDLER, J.O., WIXFORTH, A., KOSTUR, M., SCHINDLER, M. & TALKNER, P. 2004 Flow profiling of a surface-acoustic-wave nanopump. *Phys. Rev. E* 70, 056311.
- HAMILTON, M.F. & BLACKSTOCK, D.T. 1998 Nonlinear Acoustics. Academic Press.
- HASEGAWA, T., KIDO, T., IIZUKA, T. & MATSUOKA, C. 2000 A general theory of Rayleigh and Langevin radiation pressure. *J. Acoust. Soc. Japan E* 21, 146–152.
- HERTZ, G. & MENDE, H. 1939 Der Schallstrahlungsdruck in Flüssigkeiten. Z. Phys. 114, 354-367.
- HOLLY, F.J. & LEMP, M.A. 1971 Wettability and wetting of corneal epithelium. Exp. Eye Res. 11, 239-250.
- HORESH, A., KHAIKIN, D., KARNILAW, M., ZIGELMAN, A. & MANOR, O. 2019 Acoustogravitational balance in climbing films. *Phys. Rev. Fluids* 4, 022001(R).
- ISSENMANN, B., WUNENBURGER, R., MANNEVILLE, S. & DELVILLE, J.-P. 2006 Bistability of a compliant cavity induced by acoustic radiation pressure. *Phys. Rev. Lett.* **97**, 074502.
- KARLSEN, J.T., AUGUSTSSON, P. & BRUUS, H. 2016 Acoustic force density acting on inhomogeneous fluids in acoustic fields. Phys. Rev. Lett. 117, 114504.
- KING, L.V. 1934 On the acoustic radiation pressure on spheres. Proc. R. Soc. Lond. A 147, 212–240.
- LI, Y., MARCOS, J.M., FASANO, M., DIEZ, J., CUMMINGS, L.J., KONDIC, L. & MANOR, O. 2025 Using wetting and ultrasonic waves to extract oil from oil/water mixtures. *J. Colloid Interface Sci.* 700, 138442.
- LIGHTHILL, J. 1978 Acoustic streaming. J. Sound Vib. 61, 391–418.
- LONGUET-HIGGINS, M.S. 1953 Mass transport in water waves. Phil. Trans. R. Soc. Lond. A 245, 535-581
- MANOR, O., YEO, L.Y. & FRIEND, J.R. 2012 The appearance of boundary layers and drift flows due to high-frequency surface waves. J. Fluid Mech. 707, 482–495.
- MARCOS, J.M., LI, Y., FASANO, M., DIEZ, J.A., CUMMINGS, L.J., MANOR, O. & KONDIC, L. 2025 Monte Carlo-based model for the extraction of oil from oil-water mixtures using wetting and surface acoustic waves. *Phys. Rev. E* 112, 025502.
- MOROZOV, M. & MANOR, O. 2017 An extended Landau–Levich model for the dragging of a thin liquid film with a propagating surface acoustic wave. *J. Fluid Mech.* **810**, 307–322.
- MOROZOV, M. & MANOR, O. 2018 Vibration-driven mass transfer and dynamic wetting. Curr. Opin. Colloid Interface Sci. 36, 37–45.
- NAGAYAMA, K. 1996 Two-dimensional self-assembly of colloids in thin liquid films. Colloids Surf. A Physiochem. Engng Aspects 109, 363–374.
- NYBORG, W.L. 1952 Acoustic streaming due to attenuated plane waves. J. Acoust. Soc. Am. 25, 1-8.
- Oron, A., Davis, S.H. & Bankoff, S.G. 1997 Long-scale evolution of thin liquid films. *Rev. Mod. Phys.* 69, 931–980.
- OROSCO, J. & FRIEND, J. 2022 Modeling fast acoustic streaming: steady-state and transient flow solutions. *Phys. Rev. E* **106**, 045101.
- PERAZZO, C.A. & GRATTON, J. 2004 Steady and traveling flows of a power-law liquid over an incline. J. Non-Newtonian Fluid Mech. 118, 57–64.
- RAJENDRAN, V.K., ARAVIND, R.S.P. & SUBRAMANI, K. 2023 On the stability of inhomogeneous fluids under acoustic fields. *J. Fluid Mech.* **964**, A23.
- RAJENDRAN, V.K., JAYAKUMAR, S., AZHARUDEEN, M. & SUBRAMANI, K. 2022 Theory of nonlinear acoustic forces acting on inhomogeneous fluids. *J. Fluid Mech.* **940**, A32.
- RAYLEIGH, L. 1884 On the circulation of air observed in Kundt's tubes, and on some allied acoustical problems. *Phil. Trans. R. Soc. Lond.* 175, 1–21.
- REZK, A.R., MANOR, O., FRIEND, J.R. & YEO, L.Y. 2012 Unique fingering instabilities and soliton-like wave propagation in thin acoustowetting films. *Nat. Commun.* 3, 1167.
- REZK, A., MANOR, O., YEO, L. & FRIEND, J. 2014 Double flow reversal in thin liquid films driven by megahertz-order surface vibration. Proc. R. Soc. Lond. A 470, 20130765.

- ROYER, D. & DIEULESAINT, E. 1996 Elastic Waves in Solids I. Springer-Verlag.
- SCHLICHTING, H. 1932 Calculation of even periodic barrier currents. *Phys. Z.* 33, 327–335.
- SHIOKAWA, S., MATSUI, Y. & UEDA, T. 1989 Liquid streaming and droplet formation caused by leaky Rayleigh waves. Proc. IEEE Ultrason. Symp. 1, 643-646.
- SHIOKAWA, S., MATSUI, Y. & UEDA, T. 1990 Study on SAW streaming and its application to fluid devices. Japanese J. Appl. Phys. 29, 137-139.
- STOKES, G.G. 1847 On the theory of oscillatory waves. Camb. Trans. 8, 441–473.
- STONE, H.A., STROOCK, A.D. & AJDARI, A. 2004 Engineering flows in small devices. Annu. Rev. Fluid *Mech.* **36**, 381–411.
- VANNESTE, J. & BÜHLER, O. 2011 Streaming by leaky surface acoustic waves. Proc. R. Soc. Lond. A 467, 1779-1800.
- VELDHUIZEN, E.J.A. & HAAGSMAN, H.P. 2000 Role of pulmonary surfactant components in surface film formation and dynamics. Biochimica et Biophysica Acta (BBA) - Biomembranes 1467, 255-270.
- WANG, J.Z., ZHENG, Z.H., LI, H.W., HUCK, W.T.S. & SIRRINGHAUS, H. 2004 Dewetting of conducting polymer inkjet droplets on patterned surfaces. Nat. Mater. 3, 171–176.
- WHITESIDES, G.M. 2006 The origins and the future of microfluidics. *Nature* 442, 368–373.
- WIXFORTH, A. 2003 Acoustically driven planar microfluidics. Superlattices Microstruct. 33, 389–396.
- WIXFORTH, A., STROBL, C., GAUER, C., TOEGL, A., SCRIBA, J. & VON GUTTENBERG, Z. 2004 Acoustic manipulation of small droplets. Anal. Bioanal. Chem. 379, 982–991.
- YEO, L.Y. & FRIEND, J.R. 2014 Surface acoustic wave microfluidics. Annu. Rev. Fluid Mech. 46, 379-406.
- ZAREMBO, L.K. 1971 Acoustic Streaming, High-Intensity Ultrasonic Fields. Springer.